



Published in final edited form as:

Cell. 2019 April 18; 177(3): 541–555.e17. doi:10.1016/j.cell.2019.02.028.

RESIDENT MACROPHAGES CLOAK TISSUE MICROLESIONS TO PREVENT NEUTROPHIL-DRIVEN INFLAMMATORY DAMAGE

Stefan Uderhardt^{(1),(4)}, Andrew J. Martins⁽²⁾, John S. Tsang⁽²⁾, Tim Lämmermann⁽³⁾, and Ronald N. Germain⁽¹⁾

¹Lymphocyte Biology Section, Laboratory of Immune System Biology, National Institute of Allergy and Infectious Diseases, National Institutes of Health, Bethesda, MD 20892, USA

²Systems Genomics and Bioinformatics Unit, Laboratory of Immune System Biology, National Institute of Allergy and Infectious Diseases, National Institutes of Health, Bethesda, MD 20892, USA

³Max Planck Institute of Immunobiology and Epigenetics, Group Immune Cell Dynamics, 79108 Freiburg, Germany

⁴Lead contact

SUMMARY

Neutrophils are attracted to and generate dense swarms at sites of cell damage in diverse tissues, often extending the local disruption of organ architecture produced by the initial insult. Whether the inflammatory damage resulting from such neutrophil accumulation is an inescapable consequence of parenchymal cell death has not been explored. Using a combination of dynamic intravital imaging and confocal multiplex microscopy, we report here that tissue-resident macrophages rapidly sense the death of individual cells and extend membrane processes that sequester the damage, a process that prevents the initiation of the feedforward chemoattractant signaling cascade that results in neutrophil swarms. Through this “cloaking” mechanism, the resident macrophages prevent neutrophil-mediated inflammatory damage, maintaining tissue homeostasis in the face of local cell injury that occurs on a regular basis in many organs due to mechanical and other stresses.

Graphical Abstract

Correspondence: uderhardts@nih.gov (S.U.), rgermain@nih.gov (R.N.G.).

AUTHOR CONTRIBUTIONS

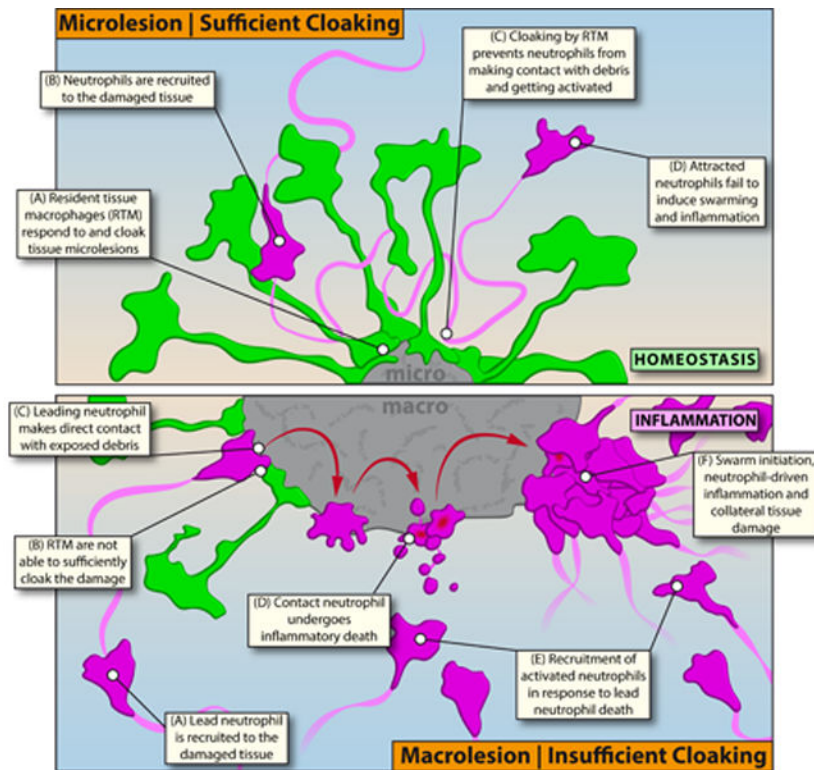
Conceptualization: S.U., T.L., R.N.G.; Investigation: S.U., A.J.M.; Formal analysis and visualization: S.U., A.J.M.; Resources: J.S.T.; Writing: S.U., R.N.G.; Supervision: R.N.G. All authors read and commented on the manuscript.

DECLARATION OF INTERESTS

The authors declare no competing interests.

DATA AND SOFTWARE AVAILABILITY

The complete set of the RNA sequencing data shown Figure 4B are available in NCBI GEO under accession number GSE119870.



INTRODUCTION

Inflammation is a multicellular host response to infectious or physical tissue damage, involving a complex, tightly orchestrated sequence of events. It begins with an initiation phase at the onset of infection or sterile cell injury, during which chemoattractant signals promote immune cell recruitment, followed by propagation and enhancement of the initial hematopoietic cell response, and ending with the eventual resolution of the lesion through clearance of the inflammatory cells and repair of the underlying tissue damage. The latter resolution event may take place with or without scarring that can disrupt optimal tissue homeostasis and function (Medzhitov, 2008). Neutrophils and recruited cells of the mononuclear phagocyte system (MPS) play pivotal roles in this sequence of events, dominating the early infiltrate and provide a critical, fast-acting layer of innate defense.

Inflammation, however, is not always beneficial to the host. Innate immune cell activation, particularly neutrophil function, is a contributing factor to different aspects of disease pathology (e.g. myocardial infarction, pneumonia) both in rodents and humans (Nicolas-Avila et al., 2017; Rock et al., 2010; Weiss, 1989). The powerful weaponry neutrophils possess to combat pathogens can cause substantial collateral damage, which then amplifies further immune cell activation, loss of functional tissue, and eventual organ dysfunction (Brandes et al., 2013). The capacity of the innate immune cellular response to increase tissue damage beyond that created by the inciting infection or lesion itself, suggests that early checkpoints controlling the inflammatory response must be in place to counter unnecessary

recruitment and secondary damage mediated by these effector cells. However, what such checkpoints might be and whether they operate merely to attenuate the magnitude or duration of otherwise typical neutrophil infiltration responses or might actually prevent such potentially tissue damaging actions of the innate immune system remain largely unknown.

Among the cells likely to play a central role in such putative regulatory activities are cells of the MPS. Macrophage transcriptional signatures are common in tissue samples from individuals or experimental animals with variety of disease processes (Murray, 2017; Wynn et al., 2013). The MPS is comprised of macrophages resident to all tissues as well as migratory monocytes that primarily circulate in the bloodstream and infiltrate tissues upon initiation of the inflammatory cascade, where they can become definitive macrophages (Geissmann et al., 2010). Fate mapping studies have revealed a strong developmental component to this dichotomy: Resident tissue macrophages (RTM) are primarily of prenatal origin (yolk sac or fetal liver), whereas monocytes are continuously produced by definitive, post-natal hematopoiesis (Ginhoux and Guilliams, 2016). Defects in the RTM compartment are often associated with developmental disorders and disruptions of physiological tissue equilibrium states (Gordon and Martinez-Pomares, 2017; Okabe and Medzhitov, 2016), highlighting the homeostatic functions executed by these macrophages, while circulating monocytes have long been implicated in the various aspects of the inflammatory cascade (Murray, 2018). However, how RTM other than brain microglial cells directly respond to tissue damage, has not been carefully explored, despite the probable contribution of such cells to regulation of local inflammatory responses (Medzhitov, 2008).

In this study, we use high-resolution intravital as well as static multi-parameter in situ imaging techniques to examine the very early stages of inflammatory responses to sterile tissue damage. We identified a regulatory mechanism that involves tissue-sessile, interstitial RTM acting as very local, dynamic first-responders to small-scale (single cell) tissue damage. By physically sequestering or “cloaking” pro-inflammatory debris, the RTM actively prevented initiation of a previously defined neutrophil recruitment and swarming cascade (Lammermann et al., 2013), thus disrupting potential tissue-damaging inflammatory responses at the earliest possible stage. Failure of the RTM-mediated cloaking process led to unchecked local inflammatory responses, neutrophil swarms, and collateral tissue damage that required secondary containment of neutrophil-driven inflammation by recruited migratory monocytes. Thus, by cloaking tissue lesions, RTM set a tissue-specific critical threshold for innate immune cell activation, constituting a previously unrecognized immune checkpoint involving the active prevention of steady-state inflammatory damage.

RESULTS

Endogenous Neutrophils Fail to Swarm at Microlesions

Neutrophil congregation is a key feature of most peripheral inflammatory responses and follows distinctive dynamic patterns described as neutrophil swarming, which comprises the recruitment and collective, directed movement of inflammatory neutrophils towards a focus in response to the prior activation of one or more “leading” neutrophils (Lammermann et al., 2013; Ng et al., 2011). To study regulatory pathways orchestrating this activation in greater detail in vivo, we developed an intravital imaging platform involving the peritoneal wall

(Figure S1A; Movie S1A). The peritoneal serosa provided a useful site with a clear anatomical structure (Figure S1B; Movie S1B) along with minimal optical and physical barriers, enabling in-depth, high-resolution imaging of inflammation and cell recruitment kinetics. This model also permitted topical application of small-molecule inhibitors or antibodies for in situ-labeling of cells (Figure S1C–S1D).

To record extravascular neutrophil dynamics, we topically applied chemokines to attract neutrophils into the peritoneum, leading to accumulation within 40–60 minutes. As expected, neutrophils displayed strong swarming behavior in response to both pathogens (Figure S1E; Movie S2A) and sterile laser-induced damage (Figure 1A; Movie S2B). In both cases, cells followed sequential activation patterns (Movie S2C–S2D): The neutrophils first approaching the damage site displayed exploratory movements (Figure 1B), followed by one or more of the cells undergoing terminal activation upon direct contact with the debris. This event was marked by distinct morphological changes and nuclear uptake of propidium iodide consistent with cell death (Figure 1B; Figure S1F–S1G). This activation was subsequently followed by the attraction of a large number of activated neutrophils directly targeted the damage, migrating in a very directed manner from many cell diameters away from the lesion site and displaying clear swarming behavior at the site of damage (Figure 1B–1C; Figure S1G–S1I). Examining the site of neutrophil swarming using auto-fluorescence and second harmonic signals over time revealed the destructive potential of this process. The recruited and aggregating neutrophils broke down the coagulated tissue but also expanded the primary damage to initially unaffected, healthy tissue, with disruption and partial destruction of collagen fibers. The result was substantial local collateral tissue damage due to the swarming response (Figure 1D; Movie S2E). These features all were consistent with prior studies in a sterile injury model in the mouse ear skin (Lammermann et al., 2013).

Given the damage that neutrophil responses to cell injury imposed, we asked if there existed discriminatory thresholds for neutrophil activation that would prevent such undesirable responses by impeding unnecessary swarming. In particular, we considered whether the accidental, non-apoptotic death of single cells, which might well be a frequent event in various tissue sites due to mechanical or other stresses (e.g. in muscles or at pleural or visceral serosal surfaces), could be prevented from routinely eliciting an inflammatory response that might contribute to progressive organ injury. To simulate such individual necrotic cell death, we scaled down the size of the laser-induced lesion to the single-cell level (= microlesion) (Figure S2A–S2D). In an initial series of experiments, we used chemoattractants to pre-elicited neutrophil migration into the tissue so that they were present at the time the stromal lesion was initiated by the laser pulse. Such extravascular neutrophils engaged in direct contact with the exposed debris (Figure S2E–S2F; Data File S1), displaying the same terminal activation patterns (Figure S2G; Movie S2F) and subsequent swarming dynamics at microlesions (Figure 1E-top) as seen with macrolesions (Figure 1E-bottom; Figure S2H; Movie S2G). Likewise, such swarming at a microlesion eventually resulted in similar collateral damage to cellular and acellular stromal components of the tissue (Figure 1F; Figure S2I; Movie S2H). Extravascular neutrophils able to rapidly access cell debris thus appeared to respond in an all-or-nothing fashion, showing similar swarming dynamics at both macro- and microlesions.

A fundamental mechanistic concept of swarming is the secretion of secondary mediators (e.g., LTB₄) by activated neutrophils, which act in a signaling relay mode to promote recruitment of inflammatory cells over longer distances within the tissue (Afonso et al., 2012; Lammermann et al., 2013). We thus sought to study not only the behavior of pre-elicited neutrophils, but to adapt our experimental setup to capture the endogenous response to the damage. Induction of a macrolesion in a naive, untreated tissue reliably drove recruitment of neutrophils within the first hour, showing delayed but similar terminal activation patterns and swarming as seen with pre-elicited neutrophils (Figure 1G; Movie S2I). However, compared to the dynamics of pre-recruited neutrophils (Figure 1H top), the endogenous response at small microlesions differed considerably (Figure 1H bottom; Movie S2J): Neutrophils were still attracted to the site of damage, but mostly displayed exploratory wandering movements and failed to undergo terminal inflammatory activation or induce swarming (Figure 1I; Figure S2J).

Resident Tissue Macrophages Cloak Tissue Microlesions

To understand why endogenously recruited neutrophils -in contrast to pre-elicited extravascular neutrophils -failed to swarm at microlesions, we investigated the dynamic behavior of other cells in the tissue. Embedded amongst fibroblasts, we found a large population of evenly distributed RTM (Figure 2A; Figure S3A; Data File S2A), which were non-migratory but whose cellular processes exhibited a continuous sampling and endocytosis behavior (Figure S3B; Movie S3A). Within 1–3 minutes of damage induction, however, RTM quickly sent out multiple spreading pseudopods towards the lesion, while still remaining sessile and fixed in position with respect to the main cell body (Figure 2B; Movie S3B).

This early dynamic response was observed in RTM within a radius of 100–150 μm around the lesion (“sensing”). Pseudopods originating from RTM within 50–100 μm eventually closed in on the outer perimeter of microlesions (“convergence”; Figure 2C), while cells further away retracted the initial probing pseudopods and continued with regular sampling dynamics. This divided the tissue and localized RTM into an inner and an outer response zone around the damage. Being numerically restricted as well as sessile with a limited radius of action, this dynamic macrophage response was far more effective at covering microlesions, where pseudopods were able to cloak all or nearly all of the visible damage (Figure 2C; Movie S3C; Data File S2B) as compared to larger regions of injury (Figure 2D). Together with the surrounding immobile stromal cells bodies, the cloaking processes covered the exposed part of the microlesion almost completely, rendering the damage functionally inaccessible to probing neutrophils (Figure 2E and 2F; Data File S2C–S2D).

At the site of lesion cloaking, large vesicles emerged indicating enhanced endocytic activity of the responding RTM (Figure 2G). This suggested that cloaking might both physically sequester the damage away from subsequently arriving neutrophils, while also scavenging damage-associated molecular products (DAMPs) released from the injured / dead cells (Uderhardt et al., 2012). Together, this inhibition of damage sensing appeared to prevent the activation and propagation of the leukotriene-dominated feed-forward recruitment sequence that is necessary for swarming (Lammermann et al., 2013).

Cloaking Prevents Neutrophil-Driven Inflammation

To test directly whether RTM cloaking actively prevents swarming, we took advantage of the fact that several RTM populations selectively express the lectin CD169 and can thus be reliably distinguished from monocytes and neutrophils (Figure S3C). The CD169-DTR mouse model allowed us to specifically deplete RTM in the peritoneum using diphtheria toxin (DT) without affecting other relevant phagocyte populations (Figure S3D–S3F).

RTM-depletion in CD169-DTR mice had no impact on the timing or extent of neutrophil recruitment, activation, and subsequent swarming at macrolesions, with comparable infiltrates within the first hours in control- and DT-treated animals (Figure 3A). Similar results were obtained with a model of acute peritonitis (Figure S3G). These results indicated that CD169-expressing RTM were not acting as sentinels of sterile insult but were dispensable for the initiation of an inflammatory response to macroscopic damage. In contrast, RTM-depletion dramatically changed the inflammatory dynamics at a microlesion: In CD169-DTR mice treated with DT to deplete the RTM and prevent cloaking, the leading neutrophils made extensive contact with the debris, underwent terminal activation, and induced swarming (Figure 3B–3C; Movie S4A;) with typical inflammatory dynamic patterns (Figure 3D; Figure S3H). These findings showed that RTM were able to prevent neutrophil swarming at microlesions, but not at macrolesions.

Quantitative Limitations to Cloaking Efficiency

Given their numeric and spatial limitations, we speculated that RTM cloaking would fail not only when the macrophages were confronted with large scale damage (macrolesions) but also when challenged with multiple microlesions at once. Indeed, two sequential microlesions set close to each other after enough time for the initial damage to begin the RTM response process allowed only the first lesion to be sufficiently cloaked, while the latter remained highly exposed. Neutrophils recruited to the uncloaked second site of damage became activated and initiated swarming, while the initial cloaked lesion maintained free of inflammation (Figure 3E; Figure S3I–S3J; Movie S4B). These observations indicate that the RTM do not provide a large-scale diffusive barrier to neutrophil activation in the tissue but act very locally to constrain neutrophil responses within the confines of their extended cellular processes at the site of tissue damage and that this response system has evolved to deal with only very limited cell damage in a local region at any one time.

When substantially depleted in a post-natal host, RTM can be replaced by monocyte precursors. The replacement cells adopt much of the tissue-specific transcriptional profile of prenatally-derived RTM over the course of several weeks, though the replacement cells do differ in some respects from the normal RTM and whether they perform an equivalent function as their pre-natal predecessors remains unclear (Ginhoux and Guillemins, 2016). We therefore used a *LysM-Cre x Csf1r-DTR* model to deplete monocytes and RTM by short-term diphtheria toxin (DT) treatment (Schreiber et al., 2013) (Figure S3E–S3F), followed by adoptive transfer of donor bone marrow cells (Figure S3K–S3L). This produced an animal with repopulation of host monocytes and new RTM, creating a chimera of host- and donor-derived macrophages in the tissue (Figure S3M). DT re-treatment 8 weeks later (Figure S3N) specifically depleted host DTR-positive macrophages without affecting donor-derived

DTR-negative RTM, creating RTM-rich and RTM-depleted areas within the same tissue, as indicated by dextran uptake (Figure S3O). As expected, donor-derived RTM readily cloaked microlesions in their vicinity (Figure 3F), while uncloaked lesions in RTM-depleted areas readily caused neutrophil swarming and inflammation (Figure 3F–3G). Taken together with the multiple lesion study, these results reveal that spatial organization and lesion density, not just size, dictate the effectiveness of RTM cloaking in response to sterile damage, rendering the inhibitory process most effective at widely spaced, individual microlesions (Figure S3P).

Sequential Sensing of Damage-Associated Alarmins Drives Cloaking

Dynamic tracking of individual RTM pseudopods from the inner and outer zone around the lesion suggested a biphasic kinetic during the cloaking response, comprising an initial sensing phase (inner and outer zone) and a subsequent convergence process (Figure 4A and 2C; Figure S4A–4B). Nucleotides act as short-range activators of innate immune cells and are among the earliest intracellular molecules released from damaged cells (Venereau et al., 2015). Transcriptional analysis of RTM revealed the expression of multiple receptors capable of sensing different nucleoside di- and/or triphosphates (Figure 4B). Removing extracellular nucleotides locally with apyrase almost completely blocked early RTM activation in response to damage and severely impaired cloaking of microlesions (Figure 4C). Targeting specific nucleotide receptors or receptor classes individually failed to interfere with cloaking and only blocking nucleotide sensing entirely could replicate the apyrase effect, which suggested a high level of receptor signaling redundancy (Figure 4C; Figure 4D).

Given the short half-life and range of extracellular nucleotides, we further speculated that other DAMPs could be involved in the full cloaking response. Pre-treatment of RTM with pertussis toxin (PT) did not interfere with initial lesion sensing but prevented the extending pseudopods from making contact with the damage, pointing to a contribution of G protein-mediated signaling during the convergence phase (Figure 4E and 4F; Figure S4B). The receptor for advanced glycation end products (RAGE) is expressed in numerous immune and non-immune cell populations, promiscuously senses a plethora of different alarmins like various AGEs, S100 family proteins, and the chromatin protein HMGB1, and operates in a predominantly PT-sensitive manner (Degryse et al., 2001). By blocking RAGE with two different pharmacological inhibitors as well as using RAGE knockout mice (Constien et al., 2001), we could indeed phenocopy the effect of PT on the convergence phase of cloaking without affecting initial sensing (Figure 4E–4G; Figure S4C).

Global RAGE-deficiency also affects inflammatory activation of neutrophils (Huebener et al., 2015). We therefore adoptively transferred wildtype and RAGE^{-/-}.eGFP bone marrow into monocyte/macrophage-depleted hosts to specifically study RAGE-deficiency on the cloaking ability of RTM (Figure S4D). Taking advantage of the non-random chimerism of host- and donor derived RTM 8 weeks after transfer, we induced microlesions in areas enriched with RAGE^{-/-} or wild type (WT) cells (Figure 4H) and directly compared their cloaking responses. RAGE-deficiency caused incomplete cloaking responses, similar to what we observed with pharmacologic inhibition (Figure 4H), eventually permitting infiltrating neutrophils to make physical contact with the debris and initiate swarm formation

(Figure 4H–4I). This data indicated that activation of RTM in response to sterile tissue damage was initiated by nucleotide-induced signaling while sensing of secondary alarmins was necessary for pseudopod extensions to complete the cloaking process.

Late Stage Events in Lesion Resolution with and without RTM Cloaking

To investigate the longer-term consequences that an absence of cloaking has on tissue homeostasis, we established an experimental system that allowed us to follow and re-image the same microlesions over time, using prominent deep vessel patterns to map the damage site (Figure 5A). At 22 hours after microlesion wounding, we consistently failed to detect neutrophil swarms in control mice (Figure 5B left), with most of the microlesions having either vanished or markedly shrunk in size (Figure 5C). Conversely, RTM-depletion in CD169-DTR mice reliably caused inflammatory swarming at microlesions that were still evident 22 hours later (Figure 5B right), with most lesions increasing in size (Figure 5C) and showing enhanced collagen displacement (Figure 5D). This indicated that lack of RTM allowed not only neutrophil-driven inflammation at microlesions but also affected healthy tissue by causing collateral damage. Cloaking, in turn, promoted healing of the microwounds in a non-phlogistic manner.

Failure of Cloaking Requires Monocyte-Recruitment and Secondary Containment

Failure of cloaking to prevent neutrophil activation at macrolesions led to recruitment of CCR2⁺ and CX3CR1⁺ monocytes 2–4 hours later (Figure S4E). Monocytes present in the tissue under steady-state conditions were migratory (Jakubzick et al., 2013), yet not primarily attracted to the damage (Figure S4F; Movie S5A). Instead, in the presence of swarming neutrophils, tissue-patrolling and recruited monocytes formed a spherical structure around the expanding focus (Figure 5E top; Movie S5B) (Dal-Secco et al., 2015; Lammermann et al., 2013), which coincided temporally with the cessation of neutrophil recruitment (Figure S4E). Systemic depletion of neutrophils abrogated monocyte attraction (Figure 5E bottom; Movie S5B), indicating that monocytes were responding to the swarming neutrophils and not the tissue damage per se. These findings suggest that if cloaking fails to prevent swarming, recruited monocytes may not only play a role in the later resolution of a lesion containing tissue and neutrophil debris but may also limit unconstrained growth of the neutrophil swarm and further tissue damage.

RTM Cloak Partially Damaged Muscle Fibers

In situ immunostaining of various serosal and interstitial tissue compartments revealed RTM populations with phenotypes and highly organized distribution patterns, similar to what we observed in the peritoneum (Figure 6A and 6B; Figure S5A, S5B and S5C). Intravital imaging of tibialis anterior muscles further showed that endo- and perimysial RTM exhibited the same dynamic cloaking response to a local necrotic tissue damage (Figure 6C) as seen in the peritoneal model. Dynamic imaging of the deeper abdominal muscles allowed careful analysis of the cellular responses after partially damaging a myocyte without killing the entire myofiber (Figure S5D). Such a damage provoked a strong cloaking response in the surrounding RTM, which sent out long processes to fully cover the damaged area of the affected myofiber (Figure 6D–6E; Data File S3). While partially damaging the myocyte caused a local swelling of the fiber, a local loss of the specific striated pattern, and the

emergence of a longitudinal striation, it did not result in complete myofiber death, with the fiber managing to retain its structural integrity (Figure S5E). Microlesions of myocytes in the presence of neutrophils, in turn, readily induced swarming and inflammation, causing further collateral damage and eventual rupture of the myofiber, highlighting the destructive power of a swarm (Figure 6F; Figure S5F) and suggesting that regulation of neutrophil-driven inflammation by RTM could be a broadly relevant mechanism of tissue protection across organs.

RTM Prevent Excess Tissue Damage Under Physiologic and Diseased Conditions

To study the role of RTM in a neutrophil-driven disease model, we employed a genetic mouse model for muscle dystrophy (mdx), in which a dystrophin deficiency leads to cellular instability, consequent necrotic damage, and eventual cell death of muscle fibers. This causes a systemic, yet self-limiting inflammatory myopathy in the first weeks of life, predominantly affecting tissues subject to higher mechanical stress like the tibialis anterior muscles or the diaphragm (Sicinski et al., 1989; Tidball, 2005). While initially only isolated myocytes are affected in the mdx model, neutrophils have been shown to play a pivotal role in exacerbating the damage and promoting clinical disease (Hodgetts et al., 2006). We hypothesized that, early in disease, interstitial RTM would respond to the isolated necrotic damage and prevent local neutrophil activation. With progressing disease, however, more necrotic events would accumulate, eventually overwhelming the tissue-protective function of RTM, leading to neutrophil activation and inflammation.

Studying the diaphragms harvested from 14 days old mdx mice revealed the early appearance of cloaking formations in the absence of neutrophil clusters (Figure S5G), often converging around local swelling of muscle fibers similar to what we observed when analyzing laser-induced myocyte damage (Figure 7A; Fig S5E). More extensive and/or advanced foci, in turn, displayed already established neutrophil-rich inflammatory responses (Figure 7A). Consistent with our predictions, early depletion of RTM after birth (using α Csfr1 treatment or the CD169DTR mouse model; Figure S3E–S3F) resulted in premature onset of disease at ages when mdx control littermates were still mostly free of muscle damage (Figure 7B–7C). Histologically, RTM-depletion in both cases led to extensive necrotic areas (Figure 7D) marked by increased neutrophil infiltrates (Figure 7E; Figure S5H), detectable in diaphragms as early as 16 days of age in RTM-depleted but not control animals (Figure S5I–S5J). Neutrophils were clearly driving this exacerbation as we were able to significantly reduce muscle necrosis in the diaphragm of mice lacking RTM by additional neutrophil depletion (Figure 7B; Figure S5K). RTM thus executed an early -yet limited -tissue-protective function in mdx mice.

We speculated that tissues subject to ongoing mechanical stress would generally be at great risk for incidental cell damage and would hence rely on tissue-protection from RTM in otherwise healthy hosts. In support of this view, we could find cloaking-like RTM constellations in peritoneal tissues of naive animals (Figure S5L) as well as to an even greater extent in diaphragm whole mounts (Figure 7F; Movie S7A). While rare at any given time (~ 5 events per diaphragm or ~ 2 per peritoneum), spontaneous cloaking clearly resembled experimentally-induced cloaking, with pseudopods converging around a central

focus, indicative of a damaged cell. In line with the notion that such ‘spontaneous’ cloaking was protecting tissues from neutrophil damage under steady-state conditions, long-term depletion of RTM in adult CD169-DTR mice led to the development of necrotic myofibers in the diaphragm associated with evidence of scattered spontaneous inflammatory damage (Figure 7G and 7H) dominated by inflammatory neutrophil infiltrates (Figure 7I; Figure S5M).

DISCUSSION

While inflammatory responses are critical to host defense, these responses can also cause extensive collateral tissue damage and hence require strict regulation to avoid disruption of organ function. While great progress has been achieved in deciphering anti-inflammatory pathways that curb propagation of ongoing responses or orchestrate active resolution of such processes (Fullerton and Gilroy, 2016), mechanisms that regulate and counter-balance the very earliest events involved in the initiation of inflammation are less well defined. This study was therefore designed to explore potential discriminatory thresholds for inflammatory responses to cell damage or death *in vivo*. Our findings provide strong evidence that tissues are not routinely subjected to damaging inflammatory responses by recruited effector cells, should parenchymal cells die due to local stresses, but rather that the initiation of neutrophil-driven inflammation is impeded through the local tissue-protective actions of sessile, tissue-resident macrophages.

Using our peritoneal imaging method, we observed rapid sensing of cell damage by RTM. This is similar to what has been observed following sterile laser damage in the brain for another population of RTM, the microglial cells (Davalos et al., 2005). As in the present report, this response depended on nucleotide stimulation of the microglial cells, while the activity of a limited nucleotide receptor set in the brain studies differed from our findings (Haynes et al., 2006), in which global inhibition of the P2X and P2Y families of receptors was necessary to impede the damage sensing mechanism. We also uncovered a key role for additional signaling events in generating the mature cloaking response of peritoneal RTM that involved the receptor RAGE, which can respond to a variety of damage-associated molecule patterns (DAMPs) such as HMGB1 or various proteins of the S100 family (Liljensiek et al., 2004). The secondary sensing by RAGE of material released from the damaged parenchymal cell was necessary for nucleotide-activated RTM to fully extend processes towards and to surround the injured or dead cell. The well-recognized role of nucleotide receptors (Cekic and Linden, 2016) and RAGE (Huebener et al., 2015) in other myeloid cells, where they can play an activating role that promotes inflammatory processes, makes it impossible to study the long-term consequences of interference with the cloaking response of RTM until animals can be engineered to selectively lack the relevant receptors in only the RTM population.

Beyond defining the ligands and receptors involved in evoking the RTM cloaking response, our investigation goes further than earlier studies to provide direct functional evidence for the important role of this macrophage response in limiting inflammatory damage in tissues under steady-state conditions. Selective depletion of RTM in CD169-DTR animals enabled microlesions to induce neutrophil swarming responses that disrupted the local cellular and

stromal tissue environment. Analysis of perfused fixed tissues revealed the presence of cloaking in naïve, unchallenged mice, suggesting a physiological role for this dynamic process. While a cloaking constellation persists only temporarily and thus is a rare event at any given time, the cumulative effects of this process over time are substantial, as prolonged RTM depletion in the CD169-DTR model led to the accumulation of necrotic myofibers in the diaphragm. This is consistent with the concept that RTM cloaking acts in the steady-state to prevent neutrophilic tissue damage in response to death of isolated cells due to mechanical and others stresses. Further evidence of the key role of the RTM cloaking process in limiting inflammatory tissue damage was obtained in a mouse model of muscle dystrophy. While monocyte-derived inflammatory macrophages have been implicated in later disease progression (Mojumdar et al., 2014), early depletion of RTM using two different approaches accelerated disease onset and severity in association with earlier than normal accumulation of extensive neutrophil infiltrates in neonatal muscles.

High resolution dynamic imaging revealed the emergence of large vesicles with centripetal movement in the pseudopods of cloaking RTM, indicative of increased endocytic activity and the removal of debris and DAMPs. Neutrophils still appeared around cloaked microlesions and showed migratory orientation towards the damage, suggesting the lesion was not “invisible”. As approaching neutrophils could be visualized directly probing the cloaking processes rather than turning away at a distance, the active secretion of chemorepulsive signals by cloaking RTM seems unlikely, though not entirely excluded. Furthermore, there was no evidence that cloaking interfered with swarm progression (after its initiation), e.g., through degradation of swarming mediators like LTB₄, as the absence of RTM did not affect early swarm establishment.

The similarities of the cloaking process to descriptions of the microglial response to laser-induced (Davalos et al., 2005) or Alzheimer’s disease-related neuronal damage (Jung et al., 2015) raise the intriguing possibility that the sequestration of DAMPs as we describe here in preventing peripheral tissue neutrophil responses might have a related function in limiting spreading of inflammatory signals in the brain, albeit without neutrophil swarming inhibition as a primary or the sole protective mechanism. Moreover, one could speculate that the cloaking actions of RTM may limit recruitment of suppressive myeloid cells in cancers but the frequent death of transformed cells in growing tumors might easily overwhelm this mechanism, leading to the type of secondary cell recruitment noted here (Franklin et al., 2014).

Swarm initiation is associated with the activation-associated death of a leading neutrophil (Lammermann et al., 2013), and we failed to find swarms being initiated without a leading neutrophil making physical contact with the lesion. Given the spatial geometry around a microlesion (Data File S2–S3), the evidence that neutrophils come close to the region of damage whether or not cloaking is present (Data File S1) and the necessity for the inflammatory death of a neutrophil to initiate swarming, we conclude that a primary function of cloaking is acute blockade of physical access to the debris, which renders cloaking a strictly local event. Blocking access prevents contact-dependent activation and death of lead neutrophils and initiation of the feedforward molecular events that produce swarming and inflammation. In turn, the more extensive the damage, the less likely it is for

RTM to prevent neutrophil contact with the damage, consistent with our experimental data. The role we reveal here for RTM in promoting tissue homeostasis and limiting cellular inflammation in response to tissue injury has likely been obscured in prior studies because RTM are easily overwhelmed in common animal models for systemic inflammatory diseases or sterile injuries by the large number of recruited cells or extent of primary damage, e.g. ischemia/infarction models, skin punch or macroscopic needle injuries. We overcame this restriction by limiting the inflammatory challenge to a single-cell damage, big enough to induce a response, but small enough to be contained by the local regulatory mechanisms.

In most tissues, RTM constitute a unique population of mostly prenatally-derived phagocytes. Early during organ development, interstitial macrophages and stromal cells establish a strong set of reciprocal interconnections that contributes to establishment of an organ-specific pattern of cell distribution and gene expression program in the local RTM population (Amit et al., 2016; Gosselin et al., 2014; Mass et al., 2016; Okabe and Medzhitov, 2014). Non-random RTM distribution patterns ensure optimal coverage and surveillance for local tissue injury, with defects in RTM population density or spatial distribution, compromising local cloaking capacity and giving attracted neutrophils a critical advantage. Perturbations of RTM population maintenance or differentiation, genetically inherited variations in RTM spatial distribution in tissues, as well as changes in body habitus due to processes such as obesity that alter the distribution pattern of these cells, may lead to a propensity for inflammatory tissue damage due to a failure of effective cloaking when cell death occurs in tissue sites with sparse local densities of RTM. In addition, there is likely gradual replacement of embryologically-derived RTM during aging with monocyte-derived cells in certain tissues (Ensan et al., 2016; Molawi et al., 2014). Further study of how the topography of RTM and the small but potentially meaningful differences in biology of fetal- vs. adult-derived RTM affects tissue homeostasis may prove informative in better understanding of the well-studied increases in measures of inflammation in the obese or elderly and of idiopathic cumulative tissue damage in certain individuals.

While RTM are deeply embedded into the stromal fabric of the tissue, migratory immune cells, such as monocytes and neutrophils, lack these intimate connections. The classical inflammatory cascade entails programs to restore -rather than preserve -tissue homeostasis (Serhan and Savill, 2005). Migratory monocytes populate peripheral tissues in meaningful numbers (10–15 % of CD11b⁺ phagocytes in the peritoneum) (Jakubzick et al., 2013). While these monocytes did not primarily respond to damage itself, they were readily attracted to ongoing swarming activity and together with additionally recruited monocytes, encircled the expanding focus as previously described. This secondary sequestering of the focus appeared to limit further neutrophil activation and recruitment and likely initiated resolving and reparative programs (Arnold et al., 2007; Dal-Secco et al., 2015). Therefore, while cooperatively tissue-protective, both RTM and monocytes play different roles in response to sterile tissue damage, namely primary prevention of inflammation and secondary resolution, respectively (Figure S5N; Movie S6).

In conclusion, our findings support a model in which RTM execute a tissue-protective role in response to acute, microscopic disruptions of stromal integrity, which can be further understood as part of the pro-homeostatic core functions of tissue macrophages, evolved to

maintain tissue and organ functionality. We speculate that tissues with limited regenerative capacity critically depend on cloaking and that defects in RTM-intrinsic cloaking factors, population dynamics, or cell distribution patterns could provoke immune responses to normally subliminal homeostatic disruptions and thus contribute to the pathogenesis of chronic inflammatory states and organ dysfunction.

STAR Methods

CONTACT FOR REAGENT AND RESOURCE SHARING

Further information and requests for resources and reagents should be directed to and will be fulfilled by the Lead Contact, Stefan Uderhardt (uderhardts@nih.gov).

Material Transfer Agreements are in place with RIKEN BRC, Japan (for CD169-DTR mice) and NYU School of Medicine, USA (for RAGE^{-/-} mice).

EXPERIMENTAL MODEL AND SUBJECT DETAILS

Animals studies—The following mouse strains were used in this study:

- *Lyz2^{gfp/gfp}* (“LysM-gfp”; C57BL/6-Lysozymetm1M-GFP; “LysM-gfp”): NIAID repository, Taconic Farms, Cat#000342;
- *Lyz2^{gfp/+}*: NIAID repository, Taconic Farms; Cat#008504.
- MaFIA (C57BL/6-Tg(Csf1r-EGFP-NGFR/FKBP1A/TNFRSF6)2Bck/J; The Jackson Laboratories; Cat#005070.
- hCD68-gfp (C57BL/6-Tg(CD68-EGFP)1Drg/J): The Jackson Laboratories; Cat#026827.
- *Lyz2^{Cre/+} Csf1r^{DTR/+}*:
 - F1 crossbreed: *Lyz2^{Cre/Cre}* (“LysM-cre”; B6.129P2-Lyz2tm1(cre)Ifo/J; The Jackson Laboratories; Cat#004781) & *Csf1r^{DTR/DTR}* (C57BL/6-Tg(Csf1r-HBEGF/mCherry)1Mnz/J; The Jackson Laboratories; Cat#024046).
- *Lyz2^{Cre/+} tdTom^{fl/+}*:
 - F1 crossbreed: *Lyz2^{Cre/Cre}* (B6.Cg-Gt(ROSA)26Sortm14(CAG-tdTomato)Hze/J; The Jackson Laboratories; Cat#007914) & *tdTom^{fl/fl}* (B6N.129P2(B6)-Lyz2tm1(cre)Ifo/J; The Jackson Laboratories; Cat#018956)
- *Siglec1^{DTR/+}* mice (B6;129-*Siglec1*<tm1(HBEGF)Mtk>; Cat#RBRC04395; Miyake et al., 2007) were kindly provided by Makoto Tanaka (Tokyo University, Japan) and distributed through Tracy McGaha (University of Toronto, Canada).
- *Siglec1^{DTR/+} Lyz2^{Cre/Cre} tdTom^{fl/fl}*
- *Cx3cr1^{gfp/+} Ccr2^{gfp/+}*;

- F1 crossbreed: *Cx3cr1^{gfp/gfp}* (C57BL/6-CD45a-[KO]CX3CR1-[KI]EGFP; Taconic Farms; Cat#008455) x *Ccr2^{flp/rlp}* (B6.129(Cg)-*Ccr2tm2.1Ifc/J*; The Jackson Laboratories; Cat#017586).
- *Dmd^{mdx}* (C57BL/10ScSn-Dmdmdx/J): The Jackson Laboratories; Cat#001801.
- *Dmd^{mdx}Lyz2^{Cre/+} tdTom^{fl/+} Siglec1^{DTR/+}*
- *Ager^{tm1.1Arnd}* (RAGE knockout; RAGE^{-/-}.eGFP) mice were kindly provided by Ann Marie Schmidt (NYU School of medicine, USA). In this mouse line, successful deletion of the RAGE gene results in transcription of eGFP (Constien et al., 2001).

All mice were maintained in specific-pathogen-free conditions at an American Association for Laboratory Animal Care–accredited animal facility at the NIAID (National Institute of Allergy and Infectious Diseases, NIH) and were used under a study protocol approved by NIAID Animal Care and Use Committee (National Institutes of Health, NIH). Mice from Taconic were obtained through a special NIAID contract.

If not otherwise stated, all imaging experiments were performed with 8–12 weeks old mice, and both male and females were used at equal ratios for the studies as they displayed similar immune cell dynamics in vivo.

METHODS DETAILS

Intravital imaging of the peritoneal serosa—See Figure S1A and Movie S1A. Intravital imaging was performed on a Zeiss 710 microscope equipped with a femtosecond-pulsed Chameleon laser (Coherent) and a 20x water immersion objective (NA 1.0, Zeiss). Animals were anesthetized with isoflurane (Baxter; FORANE; Cat#1001936040). To expose the parietal peritoneal serosa, a midline incision of the abdominal skin and peritoneal wall along the linea alba was performed. Using two small sutures (CP Medical; Monomid 5/0 Nylon; Cat#661B), the abdominal wall was carefully laid down and mounted on an 8 × 10 mm plastic base plate using Vetbond (3M; Cat#1469SB). At this point, 5–10 μl of sterile pre-warmed buffer (150 mM NaCl, 3.0 mM K, 1.4 mM Ca, 0.8 mM Mg, 1.0 P, 155 mM Cl; all chemicals were purchased from Sigma-Aldrich; pH 7.4; 34 °C) with inhibitors/vehicles or antibodies were applied topically, before installing a sterilized cover glass (Fisher Scientific; Cat# 12–545-80) flat on top of the exposed serosa. The animal was then transferred to the microscope and kept in a heated imaging chamber. The heater was adjusted so that the serosa was kept at a constant temperature of 36 °C. Animals with damage and/or bleeding due to the surgery were not studied further. Epifluorescence was used to confirm the absence of surgery-related microscopic trauma and to capture signs of premature inflammation such as vascular leakage or neutrophil rolling, in which case the animals were also not used for further experiments.

If inhibitors and/or antibodies were used, an incubation time of 25–30 minutes was added before imaging session was started. Without washing, basal macrophage dynamics were then recorded for 10 minutes prior to laser-induced damage to assess negative effects of treatments on resting activity. Experiments were only continued if macrophages exhibited regular sampling dynamics.

Data were acquired at a resolution of 512×512 (16 bit) in stacks of 12 frames each $3 \mu\text{m}$ apart at a frame rate of 968 ms using ZEN software (Zen 2012; Zeiss). For imaging, the laser was tuned to 930 nm with an output of ca. 80 mW and the following filter cubes were used: FITC/GFP (565DCXR, 525/50; Zeiss), tdTomato/RFP (565DCXR, 575–640; Zeiss), SHG (495DCLP, 447/60; Zeiss). Raw imaging data were processed and analyzed with Imaris (Bitplane). Three-dimensional tracking of cells or macrophage pseudopods was performed using Imaris to generate spatial coordinates of individual objects over time. These data were further used to calculate track displacements in Imaris or distance-time plots using a previously described open-source R script for graphic chemotaxis analysis (Lammermann et al., 2013).

Sterile laser damage—Sterile, necrotic tissue damage was induced using laser pulses to produce lesions ranging from macrolesions (5x zoom with 20x objective; brief (< 1 sec.) two photon laser pulse at ~1140 mW) to single-cell microlesions (35x zoom with 20x objective; brief (< 1 sec.) two photon laser pulse at ~380 mW). See Figure S2D.

Macrolesion: 5x zoom; damage diameter > $60 \mu\text{m}$; multicellular damage.

Microlesion: 35x zoom; damage diameter < $20 \mu\text{m}$; partial-to-unicellular damage.

RTM dynamics were recorded immediately after the laser pulse for 30 minutes (cloaking dynamics), up to 5 hours (endogenous neutrophil response) or up to 8 hours (endogenous monocyte recruitment). For inhibitor studies (Figure 4), 2–3 microlesions were set each at least $1000 \mu\text{m}$ apart. For DTR/swarming studies (Figure 3) and long-term imaging experiments (Figure 5), 5–7 microlesions were set each at least $1000 \mu\text{m}$ apart and the occurrence of swarming versus successful cloaking was recorded. The brief laser pulse coagulates the targeted tissue and causes an unmistakable, bright autofluorescence signal in virtually all imaging channels, which can be recorded over time and used to demark the lesion. Detection of a second harmonic signal was used to identify collagen structures and superficial vessels.

The IVM cloaking experiments presented in this study were performed using $\text{LysM}^{\text{gfp/gfp}}$ or $\text{LysM}^{\text{Cre/+}} \text{tdTom}^{\text{fl/+}}$ mice. Similar results were obtained using other fluorescent mouse strains such as $\text{LysM}^{\text{gfp/+}}$, MaFIA, or hCD68-gfp mice (data not shown).

Intravital imaging of tibialis anterior muscles—A similar technical setup was used for intravital imaging of tibialis anterior muscles as for the peritoneal serosa. In brief, animals were anesthetized with isoflurane, the left leg was immobilized, and a careful incision of the skin and subcutaneous tissues was performed right above the tibialis anterior muscle compartment. The epimysial fascia was carefully removed, a sterilized cover glass was installed, and imaging was performed as described above.

Intravital imaging of deep abdominal muscle tissue—The same technical setup was used to image the muscular tissue of the abdominal wall as for the peritoneal serosa, except for the imaging depth, which was around $60 - 100 \mu\text{m}$ below the peritoneal lining. Second

harmonics signals were used to visualize collagen and muscle fibers, which could readily be identified based on their characteristic striation.

***In situ* staining of neutrophils for IVM:** Gr1-FITC (BioLegend; clone RB6–8C5; Cat#108405) was washed twice in buffer using 10 kDa centrifugal filters (Millipore; Amicon Ultracel-10K; Cat#UFC501024) to remove BSA and sodium azide from the antibody solution. To label neutrophils *in situ*, ca. 0.5 µg of cleaned antibody in reconstituted in buffer was applied topically. Comparison of both neutrophil (and macrophage) dynamic behavior in the presence or absence of cleaned Gr1-FITC showed no observable difference (Figure S1C). Staining of neutrophils with Ly6G-FITC (Biolegend; clone 1A8; Cat#127605) resulted in identical staining patterns (Figure S1D) but had substantially higher background fluorescence and seemed to interfere with immune cell dynamics.

Particle uptake studies—Mice were treated intravenously with 50 µg of each BSA-AF647 (ThermoFisher; Cat#A34785), 2000 kDa Dextran-Fluorescein (Invitrogen; Cat#D7137), 70 kDa Dextran-Tetramethylrhodamine (Invitrogen; Cat#D1818) and 10 kDa Dextran-Cascade Blue (Invitrogen; Cat# D1976) diluted in 200 µl PBS. All dextrans used were lysine-fixable. Tissues were harvested 14 hours after injection and processed for confocal microscopy as described below.

Inhibitor studies—Macrophages were topically pre-treated with following inhibitors at indicated concentrations:

- Apyrase (Sigma-Aldrich; Cat#A6535): H2O; 10 U
- MRS2578 (Tocris; Cat#2146): DMSO; 10 µM
- PSB0739 (Tocris; Cat#3983): H2O; 10 µM
- Suramin (Sigma-Aldrich; Cat#S2671): H2O; 10 µM
- 5-BDBD (Tocris; Cat#3579): DMSO; 10 µM
- PSB12062 (Sigma-Aldrich; Cat#SML0753): DMSO; 10 µM
- A438079 (Sigma-Aldrich; Cat#A9736): DMSO; 100 µM
- JNJ 47965567 (Tocris; Cat#5299): DMSO; 100 µM
- isoPPADS (Tocris; Cat#0683): H2O; 100 µM
- oxATP (Sigma-Aldrich; Cat#A6779): H2O; 50 µM
- BzATP (Sigma-Aldrich; Cat#B6396): H2O; 50 µM
- FP-ZM1 (Tocris; Cat#6237): DMSO; 10 µM
- RAGE antagonist peptide (Tocris; Cat#6259): H2O; 10 µM
- Pertussis toxin (Sigma-Aldrich; Cat#P7208): H2O; 0.5 µg/ml

Animals were treated systemically (i.p.-injections) with following inhibitors:

- Clopidogrel (Sigma-Aldrich; Cat#C0614): DMSO; 1 mg/kg; 3 consecutive days.

All inhibitors were reconstituted according to the supplier's instructions and diluted in pre-warmed buffer (see above). Topical incubation volume was kept at a maximum of 10 μ l as we found that artificially increasing the interstitial volume with buffer had negative effects on macrophage sampling and cloaking dynamics, likely due to dilution of local growth factors, electrolytes and released DAMPs, respectively. After 20 minutes of incubation, intravital imaging was performed. Macrophage sampling behavior was recorded for 10 minutes, and experiments were only continued if cells displayed normal resting behavior.

2–3 micro-lesions were then induced as described above at a distance of at least 1000 μ m between each other. The dynamic response was recorded for 30 minutes after damage induction as most of the naïve or vehicle-treated cloaking dynamic was completed by that time. At least 3 animals were studied per group.

Survival surgery for long-term IVM—For long-term tracking of microlesions, vessel dyes (Dextran-Fluorescein 2000 kDa; Invitrogen; Cat#D7137) were used to identify prominent deep vessel patterns, which functioned as guiding points to map microlesions on a relative x/y-coordinate system. After damage-induction, the peritoneal cavity was closed using sutures and surgical clips, and the studied animals were allowed to wake up and recover. 22 hours later, the same animals were subjected to a second, final intravital imaging session, in which the deep vessels of the peritoneal wall were used to re-locate the lesions. At this time, Gr1-FITC was added to label infiltrating neutrophils *in situ*.

RTM depletion experiments with CD169-DTR mice—To deplete CD169-expressing RTM, CD169-DTR mice were intraperitoneally injected with vehicle or diphtheria toxin (DT; Sigma-Aldrich; Cat#D0564) every other day for five days in total (10 ng/g body weight; ~200 ng/d per mouse in 50 μ l PBS).

Tissue macrophage replacement experiments—Please see Figure S3K for experimental outline. To deplete RTM, circulating monocytes and monocyte precursors, LysM-Cre/Csf1r-DTR mice were treated with DT intraperitoneally for three days (10 ng/g body weight; ~200 ng/day per mouse in 50 μ l PBS). On the second day of treatment, 5×10^6 unsorted bone marrow cells of indicated genotypes were adoptively transferred i.v. into macrophage/monocyte-depleted hosts. Eight weeks later, the reconstituted animals displayed a non-random chimerism of repopulating host-and transferred donor-derived macrophages in the tissue, which generated host-or donor-rich areas, suitable to study the cloaking response of different RTM populations within the same tissue (e.g., Figure 4H). This setup also permitted selective depletion of the repopulating host-derived RTM (DTR-positive) by re-treating the animals with DT for three days before intravital imaging. In this case, DTR-negative donor-derived RTM were not affected by the DT, thus creating RTM-rich and RTM-depleted areas within the same tissue (Figure 3F). Where indicated, mice received dextran (10 kDa Dextran-Cascade Blue; ThermoFisher; Cat#D1976) i.v. to label tissue macrophages and confirm depletion of host-RTM on the day prior to the experiment.

Muscle dystrophy model—Mdx mice carry a mutation of the dystrophin gene (x-linked), which results in a mild myopathy starting within the first weeks after birth, characterized by an accumulation of necrotic muscle fibers and inflammatory infiltrates that

peak between day 21 and day 28 (Hodgetts et al., 2006). To evaluate the function of RTM prior to recruitment and infiltration of inflammatory cells, we thus focused on time points in which naïve mdx mice are still mostly free of disease (day 16) or start showing histological signs of disease onset (day 18).

To deplete macrophages, mdx mice were injected i.p. with vehicle or anti-CSFR1 antibodies (BioXCell; clone AFS98; Cat#BE0213) starting on day 11 (dose 0.5 mg) and repeated every other day (dose 0.25 mg) until harvest on day 16 or day 18. To specifically deplete CD169-expressing RTM in this model, mdx females were bred with CD169^{DTR/+}LysM^{Cre/Cre}tdTom^{fl/fl} males to generate DTR-positive and -negative LysM-tomato male mdx pups (x-linked). All pups were treated i.p. with DT every other day (10 ng/g body weight) starting at day 7 after birth until harvest on day 16. DTR-expression via PCR and sex was assessed post-mortem.

To deplete neutrophils, mice were additionally treated with anti-Ly6G antibodies (BioXCell; clone 1A8; Cat#BE0075-1) starting on day 15 (dose 0.25 mg) and continued every other day until the end of the experiment on day 18.

One day prior to organ harvest, mice received an i.p. injection of 0.5 % Evans blue solution (50 µl/g body weight; Tocris; Cat#0845). On the day of harvest, animals were euthanized using CO₂, tissues were collected, vigorously washed with PBS, fixed in 1 % PFA (EMS; Cat#15710) overnight at 4 °C, and further processed for confocal microscopy. Necrotic areas were measured using Imaris (Bitplane). 3–5 animals were studied per group and the experiments were repeated twice.

Peritonitis model—Mice were treated with 10 mg zymosan A (Sigma-Aldrich; Cat#Z4250) i.p. and peritoneal tissues harvested 12 hours later. Tissues were fixed in 1% PFA overnight and then stained with anti-Ly6G (BioLegend; clone 1A8). Imaris spot function was used for automated cell counting.

Immunofluorescence microscopy—Animals were euthanized with CO₂. Shortly thereafter, transcardial perfusion with pre-warmed 4% PFA (EMS; Cat#15710) was performed. Tissues were harvested and post-fixed with 12.5% BD Cytfix/Cytoperm (= 0.5 % formaldehyde; BD Bioscience; Cat#554714) for 1h at RT. Whole tissues were permeabilized with BD Perm/Wash (BD Bioscience; Cat#554723) and stained in BD Perm/Wash at RT overnight with following antibodies: CD34 PE (BioLegend; clone HM34) and CD169 A647 (BioLegend; clone 3D6.112).

Cell sorting and RNA-sequencing—One day prior to the experiment, *Cx3cr1^{gfp/+} Ccr2^{flp/+}* animals received an i.v. injection of 50 µg Dextran-Cascade Blue (Invitrogen; Cat#D1976) to label interstitial phagocytes. On the day of the experiment, mice received 1 µg anti-CD45 (BioLegend; clone 30-F11) intravenously 3 minutes prior to euthanasia in order to label intravascular leukocytes. The peritoneal wall was then carefully removed, spread out in a 6-well plate, and covered with 2.5 ml dissociation buffer: RPMI (Gibco; Cat#11875093); 1% FBS (Gemini; Lot#A20G001; Cat#100-106); 250 µg/ml Liberase TL (Sigma-Aldrich; Cat#5401020001); 100 µg/ml DNase II (Sigma-Aldrich; Cat#

D8764); 25 μ M Z-VAD-FMK (Tocris; Cat#2163); 10 mM HEPES (Gibco; Cat#15630080). After 20 minutes of incubation at 37 °C, dissociation was stopped with ice-cold FACS-buffer: PBS (Gibco; Cat#10010-23; Lot#1943335); 2% FBS, 2 mM EDTA (Quality Biological; Cat#51-027-101). The most superficial tissue layers were gently scraped off the underlying abdominal wall using a plastic cell scraper and forced through a 70 μ m cell strainer. Cells were resuspended in buffer containing 25 μ M Z-VAD-FMK and stained with antibodies for CD11b (BioLegend; clone M1/70), I-A/I-E (BioLegend; clone M5/114.15.2) and Ly6G (BioLegend; clone 1A8). CD45⁻CD11b⁺Ly6G⁻ cells were sorted into Dextran⁺MHCII⁻CCR2⁻CX3CR1⁻ (majority of sessile RTM; 85–90 % of CD11b⁺Ly6G⁻ cells), MHCII⁺CCR2⁺CX3CR1⁻ (migratory tissue monocytes; 10–15 %) and MHCII⁺CCR2⁻CX3CR1⁺ (sessile RTM; 0.5–1.5 %) populations, directly into 0.5 ml TRIZOL (Invitrogen; Cat#15596026) using a FACS-Aria cell sorter (BD Bioscience).

RNAseq libraries were prepared using the Nugen Ovation SoLo (NuGEN; Cat#0501-32) with ~1 ng total RNA input. Sequencing was performed using Illumina NextSeq V2 reagents (Illumina; Cat#FC-404-2005) using paired end 75 base pair reads. Samples were sequenced to a depth of ~20 million reads. Reads were mapped to the *Mus musculus mm10* genome build (UCSC annotation) using Salmon. Salmon-estimated transcripts-per-million (TPM) values were summarized at the gene level using tximport version 1.4.0 and the org.Mm.eg.db database. Data shown in Figure 4B are pooled from three independent biological replicates.

Generation of Planar Sections or Interactive 3D Models (“Data File S1–S3”)—IVM still images were taken on a Zeiss LSM 710 microscope at the Nyquist sampling rate (“optimal” resolution setting in ZEN 2012), and Huygens Professional (18.04; Scientific Volume Imaging) was used for deconvolution at default parameters. 3D surface models were generated in IMARIS (Bitplane) using default parameters. Individual models were exported from IMARIS as wrl-files and imported into MeshLab (ISTI-CNR). To generate x/y/z slices of the 3D models, individual planar sections were computed in MeshLab and exported as wrl-meshes, pseudocolored and assembled as a 3D-model using Photoshop (Adobe), which was then exported as a u3d-file and implemented into a pdf-file using Adobe Acrobat Pro DC. To generate interactive multi-layer 3D models, individual surface models were first simplified in MeshLab for better handling using clustering decimation (at 0.5 %), and exported again as wrl-files. Individual mesh models were imported into Photoshop, assembled, pseudo-colored, exported as u3d-files and inserted into a .pdf-file using Adobe Acrobat Pro DC.

To view and interact with the multi-layer 3D model in the “Data File”, the .pdf-file needs to be opened with Adobe Acrobat Reader (<https://get.adobe.com/reader/>), as other pdf-viewers (e.g. Preview on macOS) don’t support this function. Once opened, click on the model to activate the animation. If prompted, click on “Trust this document”. If the 3D model is not visible, enable 3D content under “Preferences > 3D & Multimedia > Enable playing of 3D content”. See page 2 of Data File S1–S3 for visual instructions. For further help and troubleshooting, please visit <https://helpx.adobe.com/acrobat/using/displaying-3d-models-pdfs.html>.

To interact with the model, click next to it and hold to freely rotate (see movie on page 3 of Data File S2 for demonstration). On Mac hold the <option> and <command> keys and use the scroll function of your mouse to zoom in or out (Windows: hold the <Alt> key and scroll). The “Model tree” lists the individual parts of the model. Here you can hide different parts by clicking the box, or make parts transparent by clicking on the part and selecting “Transparent” from the “Options” menu above.

Tissue clearing and whole mount imaging—Mice were sacrificed and immediately perfused with 20 ml 4 % PFA over 15 minutes. Diaphragms were harvested and post-fixed with 0.5 % PFA overnight at 4° C. On next day, tissues were washed extensively with PBS, and subsequently stained with Wheat Germ Agglutinin AF488 (10 µg/ml; ThermoFisher; Cat#W11261) diluted in PBS overnight at room temperature. On next day, excess fluids were removed and tissues were transferred into freshly prepared Ce3D-clearing medium. Ce3D-clearing medium was prepared as previously described (Li et al., 2017). In brief, 4 g Histodenz (Sigma-Aldrich; Cat#D2158) were dissolved in 2.75 ml 40 % N-Methylacetamide (Sigma-Aldrich; Cat#M26305) and 5 µl Triton X-100 (Sigma-Aldrich; Cat#T8787) on a rotator for 2 hours at 37° C. Diaphragms were transferred into the clearing medium and incubated for 2 days on a tube rotator at room temperature. Next, tissues were mounted on glass slides and confocal imaging was performed on an inverted SP8 microscope (Leica Microsystems) using a 20× 0.75NA objective at a 512×512 resolution at 2.5x optical zoom, with voxel size of 0.45 µm in the lateral and 1.5 µm in the axial direction.

Assessment of spontaneous cloaking—Frequency of spontaneous cloaking in diaphragm tissues (= 4.94 per whole diaphragm) was calculated based on confocal imaging data obtained from cleared whole mount diaphragms of five naïve, perfusion-fixed *Lyz2^{Cre/+}tdTom^{fl/+}* mice (mixed sex; 12–16 weeks) with an average whole tissue volume of 105.7 mm³ and an average number of macrophages of 804,582 per diaphragm.

Frequency of spontaneous cloaking in peritoneal tissues (= 2.09 per whole peritoneum) was calculated based on multiphoton imaging data obtained from eight *LysM^{gfp/gfp}* mice (mixed sex; 10–16 weeks), which, after perfusion-fixation, were prepared as for intravital imaging to avoid artificial damaging of the tissue. As only RTM in the narrow submesothelial space were imaged and counted, the number of cloaking findings was calculated per area of peritoneal tissue (with an average area of 1314 mm² of the peritoneum lining the abdominal wall and an average of 748.352 submesothelial RTM per abdominal peritoneum), neglecting the deeper muscular tissues.

QUANTIFICATION AND STATISTICAL ANALYSIS

No statistical methods were used to predetermine sample sizes. Statistical analyses were performed with Prism 7 (GraphPad Software). Results are presented as means ± SEM and exact P values are depicted in the figures. Unpaired student’s t-test (two-tailed), or one-way or two-way ANOVA tests were performed to compare two or more groups after data were confirmed to be normally distributed. Where applicable, post-hoc multiple comparison tests were performed (Tukey for pairs, Bonferroni for multiple groups). Paired data from the

long-term imaging experiments were analyzed using Wilcoxon matched-pairs signed rank tests.

Supplementary Material

Refer to Web version on PubMed Central for supplementary material.

ACKNOWLEDGEMENT

We are grateful to M. Tanaka and T. McGaha for providing CD169-DTR mice, and A.M. Schmidt for providing RAGE mice.

We thank the members of the R.N.G. laboratory and the Laboratory of Immune System Biology (LISB) for comments and discussions, and A. R umenapf for proofreading. This work was supported by the Intramural Research Program of National Institute of Allergy and Infectious Diseases, NIH. S.U. received a stipend from the Deutsche Forschungsgemeinschaft DFG (UD 84/1-1).

REFERENCES

- Afonso PV, Janka-Junttila M, Lee YJ, McCann CP, Oliver CM, Aamer KA, Losert W, Cicerone MT, and Parent CA (2012). LTB4 is a signal-relay molecule during neutrophil chemotaxis. *Dev Cell* 22, 1079–1091. [PubMed: 22542839]
- Amit I, Winter DR, and Jung S (2016). The role of the local environment and epigenetics in shaping macrophage identity and their effect on tissue homeostasis. *Nat Immunol* 17, 18–25. [PubMed: 26681458]
- Arnold L, Henry A, Poron F, Baba-Amer Y, van Rooijen N, Plonquet A, Gherardi RK, and Chazaud B (2007). Inflammatory monocytes recruited after skeletal muscle injury switch into antiinflammatory macrophages to support myogenesis. *J Exp Med* 204, 1057–1069. [PubMed: 17485518]
- Brandes M, Klauschen F, Kuchen S, and Germain RN (2013). A systems analysis identifies a feedforward inflammatory circuit leading to lethal influenza infection. *Cell* 154, 197–212. [PubMed: 23827683]
- Cekic C, and Linden J (2016). Purinergic regulation of the immune system. *Nat Rev Immunol* 16, 177–192. [PubMed: 26922909]
- Constien R, Forde A, Liliensiek B, Grone HJ, Nawroth P, Hammerling G, and Arnold B (2001). Characterization of a novel EGFP reporter mouse to monitor Cre recombination as demonstrated by a Tie2 Cre mouse line. *Genesis* 30, 36–44. [PubMed: 11353516]
- Dal-Secco D, Wang J, Zeng Z, Kolaczowska E, Wong CH, Petri B, Ransohoff RM, Charo IF, Jenne CN, and Kubes P (2015). A dynamic spectrum of monocytes arising from the in situ reprogramming of CCR2+ monocytes at a site of sterile injury. *J Exp Med* 212, 447–456. [PubMed: 25800956]
- Davalos D, Grutzendler J, Yang G, Kim JV, Zuo Y, Jung S, Littman DR, Dustin ML, and Gan WB (2005). ATP mediates rapid microglial response to local brain injury in vivo. *Nat Neurosci* 8, 752–758. [PubMed: 15895084]
- Degryse B, Bonaldi T, Scaffidi P, Muller S, Resnati M, Sanvito F, Arrigoni G, and Bianchi ME (2001). The high mobility group (HMG) boxes of the nuclear protein HMG1 induce chemotaxis and cytoskeleton reorganization in rat smooth muscle cells. *J Cell Biol* 152, 1197–1206. [PubMed: 11257120]
- Ensan S, Li A, Besla R, Degousee N, Cosme J, Roufaiel M, Shikatani EA, El-Maklizi M, Williams JW, Robins L, et al. (2016). Self-renewing resident arterial macrophages arise from embryonic CX3CR1(+) precursors and circulating monocytes immediately after birth. *Nat Immunol* 17, 159–168. [PubMed: 26642357]
- Franklin RA, Liao W, Sarkar A, Kim MV, Bivona MR, Liu K, Pamer EG, and Li MO (2014). The cellular and molecular origin of tumor-associated macrophages. *Science* 344, 921–925. [PubMed: 24812208]

- Fullerton JN, and Gilroy DW (2016). Resolution of inflammation: a new therapeutic frontier. *Nat Rev Drug Discov* 15, 551–567. [PubMed: 27020098]
- Geissmann F, Manz MG, Jung S, Sieweke MH, Merad M, and Ley K (2010). Development of monocytes, macrophages, and dendritic cells. *Science* 327, 656–661. [PubMed: 20133564]
- Ginhoux F, and Williams M (2016). Tissue-Resident Macrophage Ontogeny and Homeostasis. *Immunity* 44, 439–449. [PubMed: 26982352]
- Gordon S, and Martinez-Pomares L (2017). Physiological roles of macrophages. *Pflugers Arch* 469, 365–374. [PubMed: 28185068]
- Gosselin D, Link VM, Romanoski CE, Fonseca GJ, Eichenfield DZ, Spann NJ, Stender JD, Chun HB, Garner H, Geissmann F, et al. (2014). Environment drives selection and function of enhancers controlling tissue-specific macrophage identities. *Cell* 159, 1327–1340. [PubMed: 25480297]
- Haynes SE, Hollopeter G, Yang G, Kurpius D, Dailey ME, Gan WB, and Julius D (2006). The P2Y12 receptor regulates microglial activation by extracellular nucleotides. *Nat Neurosci* 9, 1512–1519. [PubMed: 17115040]
- Hodgetts S, Radley H, Davies M, and Grounds MD (2006). Reduced necrosis of dystrophic muscle by depletion of host neutrophils, or blocking TNFalpha function with Etanercept in mdx mice. *Neuromuscul Disord* 16, 591–602. [PubMed: 16935507]
- Huebener P, Pradere JP, Hernandez C, Gwak GY, Caviglia JM, Mu X, Loike JD, Jenkins RE, Antoine DJ, and Schwabe RF (2015). The HMGB1/RAGE axis triggers neutrophil-mediated injury amplification following necrosis. *J Clin Invest* 125, 539–550. [PubMed: 25562324]
- Jakubzick C, Gautier EL, Gibbings SL, Sojka DK, Schlitzer A, Johnson TE, Ivanov S, Duan Q, Bala S, Condon T, et al. (2013). Minimal differentiation of classical monocytes as they survey steady-state tissues and transport antigen to lymph nodes. *Immunity* 39, 599–610. [PubMed: 24012416]
- Jung CK, Keppler K, Steinbach S, Blazquez-Llorca L, and Herms J (2015). Fibrillar amyloid plaque formation precedes microglial activation. *PLoS One* 10, e0119768. [PubMed: 25799372]
- Lammermann T, Afonso PV, Angermann BR, Wang JM, Kastenmuller W, Parent CA, and Germain RN (2013). Neutrophil swarms require LTB4 and integrins at sites of cell death in vivo. *Nature* 498, 371–375. [PubMed: 23708969]
- Li W, Germain RN, and Gerner MY (2017). Multiplex, quantitative cellular analysis in large tissue volumes with clearing-enhanced 3D microscopy (Ce3D). *Proc Natl Acad Sci U S A* 114, E7321–E7330. [PubMed: 28808033]
- Liliensiek B, Weigand MA, Bierhaus A, Nicklas W, Kasper M, Hofer S, Plachky J, Grone HJ, Kurschus FC, Schmidt AM, et al. (2004). Receptor for advanced glycation end products (RAGE) regulates sepsis but not the adaptive immune response. *J Clin Invest* 113, 1641–1650. [PubMed: 15173891]
- Mass E, Ballesteros I, Farlik M, Halbritter F, Gunther P, Crozet L, Jacome-Galarza CE, Handler K, Klughammer J, Kobayashi Y, et al. (2016). Specification of tissue-resident macrophages during organogenesis. *Science* 353.
- Medzhitov R (2008). Origin and physiological roles of inflammation. *Nature* 454, 428–435. [PubMed: 18650913]
- Miyake Y, Asano K, Kaise H, Uemura M, Nakayama M, and Tanaka M (2007). Critical role of macrophages in the marginal zone in the suppression of immune responses to apoptotic cell-associated antigens. *J Clin Invest* 117, 2268–2278. [PubMed: 17657313]
- Mojumdar K, Liang F, Giordano C, Lemaire C, Danialou G, Okazaki T, Bourdon J, Rafei M, Galipeau J, Divangahi M, et al. (2014). Inflammatory monocytes promote progression of Duchenne muscular dystrophy and can be therapeutically targeted via CCR2. *EMBO Mol Med* 6, 1476–1492. [PubMed: 25312642]
- Molawi K, Wolf Y, Kandalla PK, Favret J, Hagemeyer N, Frenzel K, Pinto AR, Klapproth K, Henri S, Malissen B, et al. (2014). Progressive replacement of embryo-derived cardiac macrophages with age. *J Exp Med* 211, 2151–2158. [PubMed: 25245760]
- Murray PJ (2017). Macrophage Polarization. *Annu Rev Physiol* 79, 541–566. [PubMed: 27813830]
- Murray PJ (2018). Immune regulation by monocytes. *Semin Immunol* 35, 12–18. [PubMed: 29290545]

- Ng LG, Qin JS, Roediger B, Wang Y, Jain R, Cavanagh LL, Smith AL, Jones CA, de Veer M, Grimbaldeston MA, et al. (2011). Visualizing the neutrophil response to sterile tissue injury in mouse dermis reveals a three-phase cascade of events. *J Invest Dermatol* 131, 2058–2068. [PubMed: 21697893]
- Nicolas-Avila JA, Adrover JM, and Hidalgo A (2017). Neutrophils in Homeostasis, Immunity, and Cancer. *Immunity* 46, 15–28. [PubMed: 28099862]
- Okabe Y, and Medzhitov R (2014). Tissue-specific signals control reversible program of localization and functional polarization of macrophages. *Cell* 157, 832–844. [PubMed: 24792964]
- Okabe Y, and Medzhitov R (2016). Tissue biology perspective on macrophages. *Nat Immunol* 17, 9–17. [PubMed: 26681457]
- Rock KL, Latz E, Ontiveros F, and Kono H (2010). The sterile inflammatory response. *Annu Rev Immunol* 28, 321–342. [PubMed: 20307211]
- Schreiber HA, Loschko J, Karssemeijer RA, Escolano A, Meredith MM, Mucida D, Guermonez P, and Nussenzweig MC (2013). Intestinal monocytes and macrophages are required for T cell polarization in response to *Citrobacter rodentium*. *J Exp Med* 210, 2025–2039. [PubMed: 24043764]
- Serhan CN, and Savill J (2005). Resolution of inflammation: the beginning programs the end. *Nat Immunol* 6, 1191–1197. [PubMed: 16369558]
- Sicinski P, Geng Y, Ryder-Cook AS, Barnard EA, Darlison MG, and Barnard PJ (1989). The molecular basis of muscular dystrophy in the mdx mouse: a point mutation. *Science* 244, 1578–1580. [PubMed: 2662404]
- Tidball JG (2005). Inflammatory processes in muscle injury and repair. *Am J Physiol Regul Integr Comp Physiol* 288, R345–353. [PubMed: 15637171]
- Uderhardt S, Herrmann M, Oskolkova OV, Aschermann S, Bicker W, Ipseiz N, Sarter K, Frey B, Rothe T, Voll R, et al. (2012). 12/15-lipoxygenase orchestrates the clearance of apoptotic cells and maintains immunologic tolerance. *Immunity* 36, 834–846. [PubMed: 22503541]
- Venereau E, Ceriotti C, and Bianchi ME (2015). DAMPs from Cell Death to New Life. *Front Immunol* 6, 422. [PubMed: 26347745]
- Weiss SJ (1989). Tissue destruction by neutrophils. *N Engl J Med* 320, 365–376. [PubMed: 2536474]
- Wynn TA, Chawla A, and Pollard JW (2013). Macrophage biology in development, homeostasis and disease. *Nature* 496, 445–455. [PubMed: 23619691]

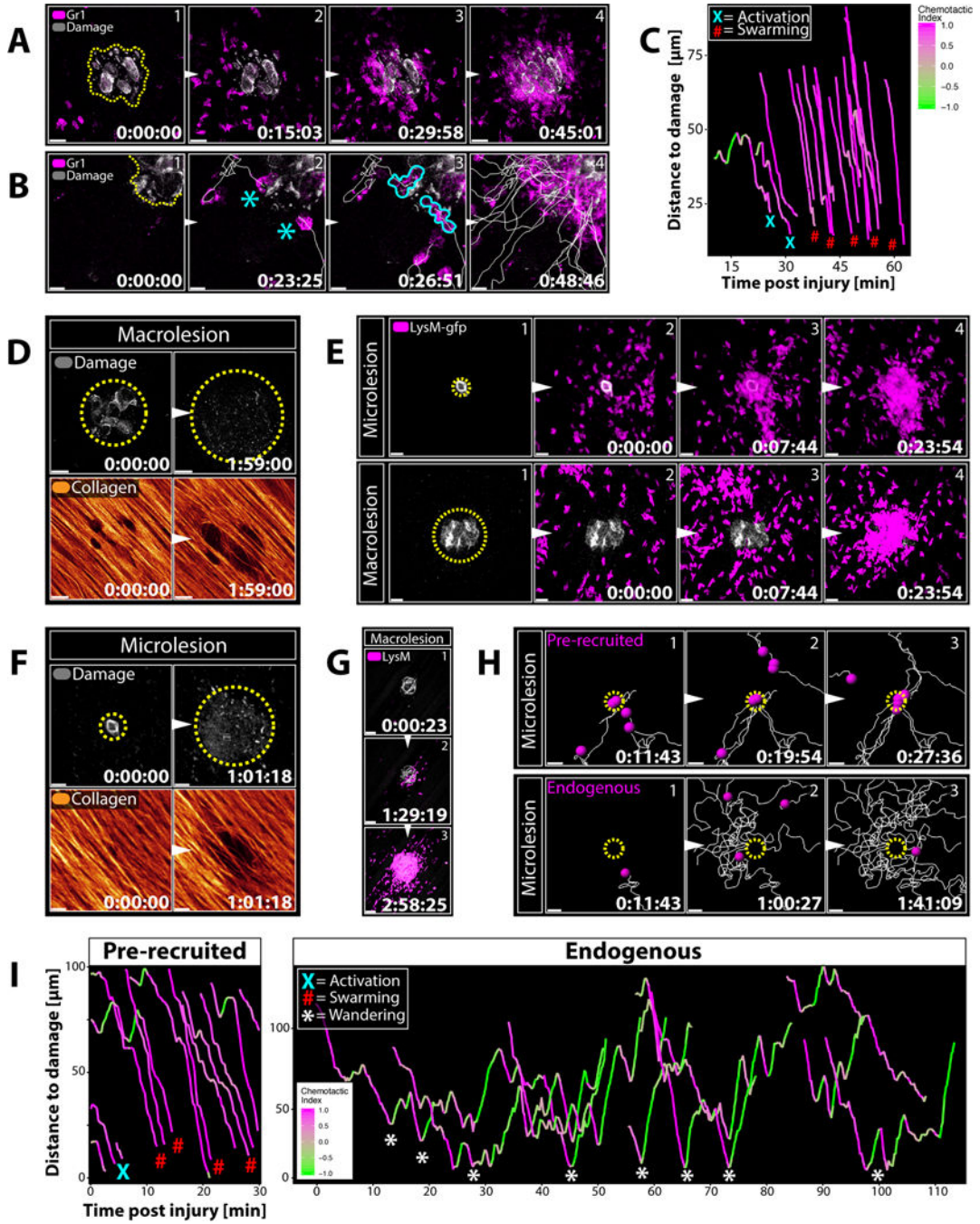


Figure 1. Endogenous Neutrophils Fail to Swarm at Microlesions.

A) Pre-recruited neutrophils (magenta) swarming at a macrolesion (grey). Scale bar, 30 μm . Representative of 3 experiments. See Movie S2B.

B) Leading neutrophils (magenta) undergo cell death (cyan outline) upon contact (*) with macrolesion (grey) and initiate swarming. Scale bar, 10 μm . See Movie S2C.

C) Distance-time plot of individual tracks of pre-recruited neutrophils migrating towards a macrolesion (bottom of the graph). Track color = chemotactic index; X = neutrophil death; # = swarming. Representative of 3 experiments. See Figure S1H.

D) Changes in injury size (top; grey) and collagen structure (bottom) at a macrolesion with pre-recruited neutrophils over time. Scale bar, 30 μm . Representative of 2 experiments. See Movie S2E.

E) Pre-recruited neutrophils (magenta) swarming at a macrolesion (top) or a microlesion (bottom). Scale bar, 30 μm . Representative of 4 experiments. See Movie S2G.

F) Changes in injury size (top; grey) and collagen structure (bottom) at a microlesion with pre-recruited neutrophils over time. Scale bar, 30 μm . Representative of 3 experiments. See Movie S2H.

G) Swarming behavior of endogenously recruited neutrophils (magenta) at a macrolesion (grey). Scale bar, 50 μm . Representative of 2 experiments. See Movie S2I.

H) Individual tracks of pre-recruited (top) versus endogenously recruited neutrophils (bottom) at microlesions (outline). Scale bar, 20 μm . Representative of 3 experiments. See Movie S2J.

I) Distance-time plot of tracks of pre-recruited (left) vs. endogenously recruited (right) neutrophils migrating towards a microlesion. Track color = chemotactic index; **X** = neutrophil death; # = swarming; * = wandering behavior. See Figure S1H. Representative of 3 experiments. See Movie S2J.

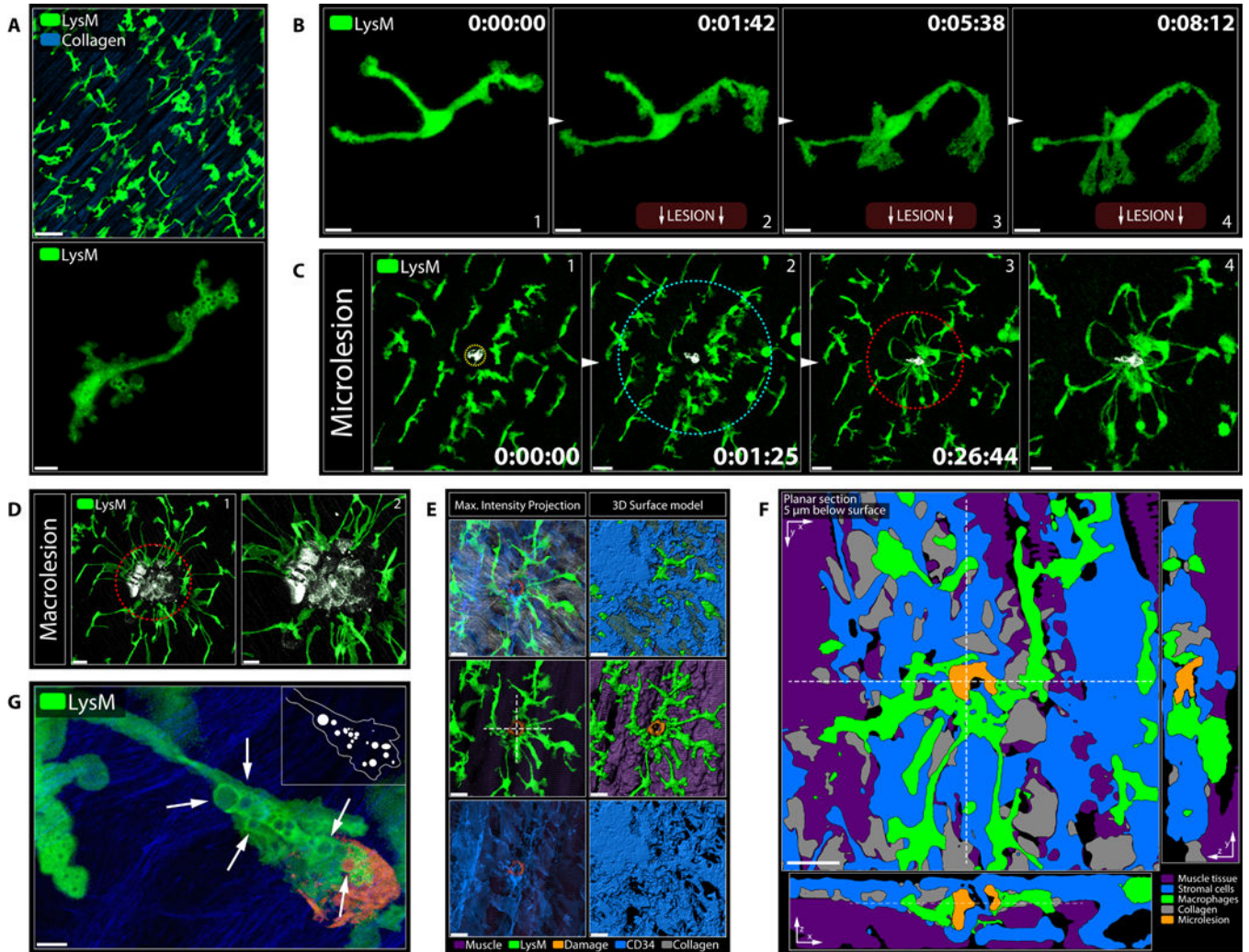


Figure 2. Resident Tissue Macrophages are Dynamic First Responders to Tissue Damage.
 A) Peritoneal serosa (top) and close-up image of an RTM (bottom) under resting conditions. Scale bars, 5 μ m (top) and 50 μ m (bottom). See Movie S3A.
 B) First minutes of an individual RTM (green) responding to a sterile tissue injury (bottom; not shown). Scale bar, 10 μ m. See Movie S3B.
 C) RTM (green) responding to a microlesion (grey). Image (4) shows (3) in higher magnification. Circles indicate inner (red) and outer (cyan) response zone around the damage. Scale bars, 20 μ m (1–3) and 10 μ m (4). See Movie S3C.
 D) Different magnifications of RTM (green) responding to a macrolesion (grey). Scale bars, 20 μ m (left) and 10 μ m (right).
 E) Cloaking RTM and stromal cells covering a microlesion. Max intensity projection (left); 3D surface model (right). See Data File S2C. Scale bar, 20 μ m. Dashed cross marks cross section in Figure 2F. Representative of > 5 experiments.
 F) Planar cross sections of 3D object in Figure 2E. See Data File S2D. Scale bar, 20 μ m.
 G) Large endosomes (arrows) in a cloaking RTM (green) at a microlesion (orange). Scale bar, 5 μ m.

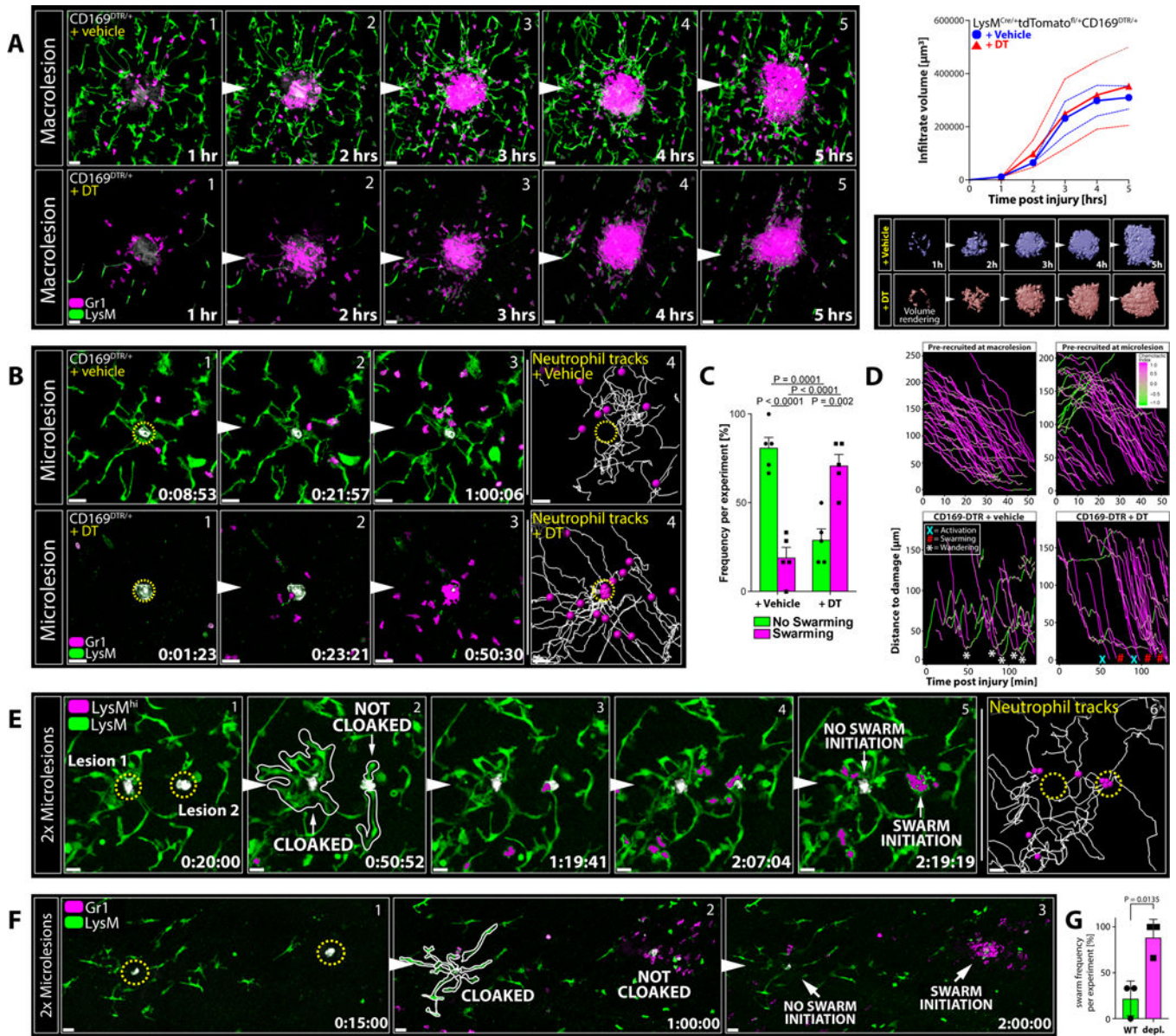


Figure 3. Cloaking by RTM Prevents Neutrophil Activation and Subsequent Swarming.
 A) RTM (green) and neutrophils (magenta) responding to macrolesions (grey) in CD169-DTR mice treated with vehicle (top; blue graph) or DT (bottom; red graph). Scale bar, 30 µm. Graphs show infiltrate volumes (means ± SEM as dashed lines) over time. Bottom pictures show surface volume renderings of infiltrates. n = 4 animals per group.
 B) RTM (green) and neutrophils (magenta) responding to microlesions (grey) in CD169-DTR mice treated with vehicle (top) or DT (bottom). Scale bar, 30 µm. n = 5 animals per group. See Movie S4A.
 C) Frequencies of neutrophil swarming (magenta) versus successful cloaking by RTM (= no swarming; green) at microlesions in vehicle-(left) or DT-treated (right) CD16-DTR mice. Two-way ANOVA; n = 5 animals per group with 5–7 microlesions per mouse; means ± SEM.
 D) Neutrophil tracks at macrolesion and microlesion for CD169-DTR + vehicle and + DT. Distance to damage (µm) is plotted against time post injury (min). Legend: Activation (X), Swarming (Y), Wandering (Z).
 E) Cloaking of two microlesions. NOT CLOAKED and CLOAKED states are shown. SWARM INITIATION and NO SWARM INITIATION are also indicated. Neutrophil tracks are shown in yellow.
 F) Cloaking of two microlesions. CLOAKED, NOT CLOAKED, NO SWARM INITIATION, and SWARM INITIATION states are shown.
 G) Swarming frequency per experiment [%] for WT depl. P = 0.0135.

D) Top: Distance-time plot showing tracks of pre-recruited neutrophils migrating towards a macro-(top left) or microlesion (top right). Bottom: Distance-time plot showing individual tracks of endogenously recruited neutrophils migrating towards a microlesion in vehicle-(bottom left) or DT-treated (right) CD169-DTR mice. **X** = neutrophil death; # = swarming; * = wandering behavior. See Figure S1H.

E) RTM (green) and neutrophils (green/magenta) responding to two sequential microlesions (grey) set close to each other at minute 0 (left lesion 1) and at minute 20 (right lesion 2). Scale bar, 20 μm . Representative of 3 experiments. See Movie S4B.

F) RTM (green) and neutrophils (magenta) responding to two micro-lesions set simultaneously in an RTM-rich (left lesion) or RTM-lacking (right lesion) area in partially RTM-depleted mice. Scale bar, 30 μm . Representative of 3 experiments with 3 sets of lesions per mouse. See Figure S3K–S3O.

G) Frequency of neutrophil swarm initiations in RTM-rich (WT) versus RTM-depleted (depl.) areas within the same field-of-view (Figure 3F). Unpaired t test; n = 3 animals per group with 3 microlesion sets per mouse; means \pm SEM.

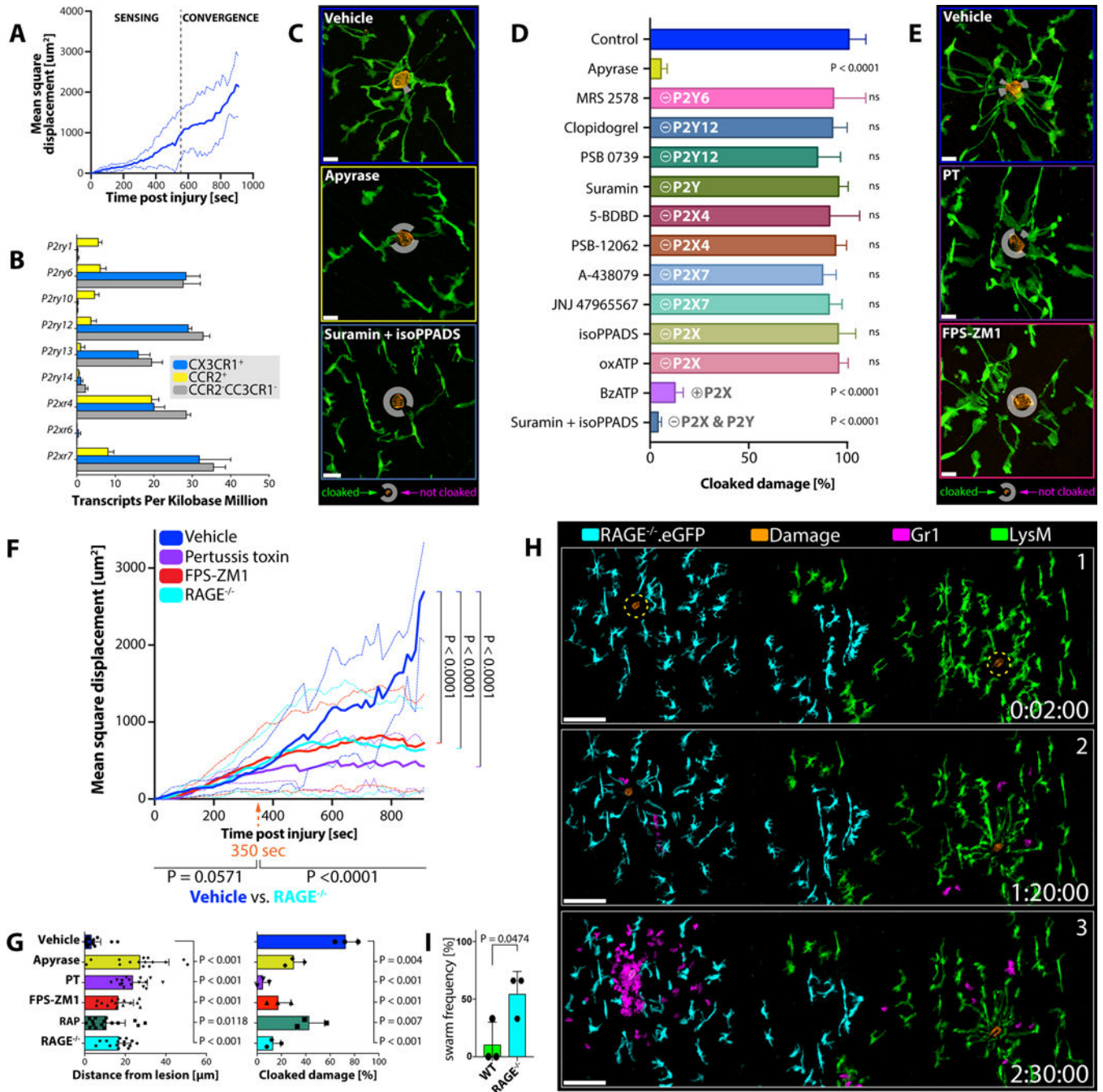


Figure 4. Sequential Sensing of Damage-Associated Alarmins Drives Cloaking.

A) Mean square displacement of individual RTM pseudopods moving towards a micro-lesion over time. Data pooled from three independent tracking experiments. See Figure S4A–S4B.

B) P2 receptor expression in different phagocyte populations isolated from peritoneal tissues of *Cx3cr1^{gfp/+} Ccr2^{flp/+}* mice (n = 3). Normalized reads per kilobases; means ± SEM.

C) RTM (green) responses 30 minutes after damage induction (orange) in mice pre-treated with vehicle (top), apyrase (mid) or suramin/isoPPADS (bottom). n = 3–5 animals per group with 2–3 lesions per mouse. Scale bar, 15 μ m. White circles mark un-cloaked areas.

D) Comparison of RTM cloaking capacities upon inhibitor treatment. n = 2–3 animals per group with 2–3 lesions per mouse. One-way ANOVA; each condition compared to the naïve control; means \pm SEM.

E) RTM (green) responses 30 minutes after damage (orange) induction in mice treated with vehicle (top), PT (mid) or FPS-ZM1 (bottom). n = 3–5 animals per group with 2–3 lesions per mouse. Scale bar, 15 μ m.

F) Mean square displacement of individual RTM pseudopods moving towards a microlesion in WT mice treated with vehicle (blue), FPS-ZM1 (red) or pertussis toxin (purple), and RAGE^{-/-} (cyan) mice over time. Data pooled from three independent tracking experiments for each condition. Two-way ANOVA; means \pm SEM. See Figure S4C.

G) Distances of pseudopods to microlesions (left) and physically cloaked area (right; pooled data from three independent experiments) 30 minutes after damage induction in WT mice treated with vehicle (blue), apyrase (yellow), pertussis toxin (PT; purple), FPS-ZM1 (red) or RAGE Antagonist Peptide (RAP; green), or RAGE^{-/-} (cyan) mice. Two-way ANOVA; means \pm SEM. See Figure S4C.

H) Responses of wildtype RTM (green) versus RAGE^{-/-}.eGFP RTM (cyan) to simultaneously induced microlesions (orange) and subsequent neutrophil behavior (magenta). See Figure S4D. Scale bar, 100 μ m. Representative of 3 experiments with 3 sets of lesions per mouse.

I) Frequency of neutrophil swarm initiations in wild type (WT) versus RAGE-deficient (RAGE^{-/-}) areas. Unpaired t test; n = 3 animals per group with 3 lesion sets per mouse; means \pm SEM.

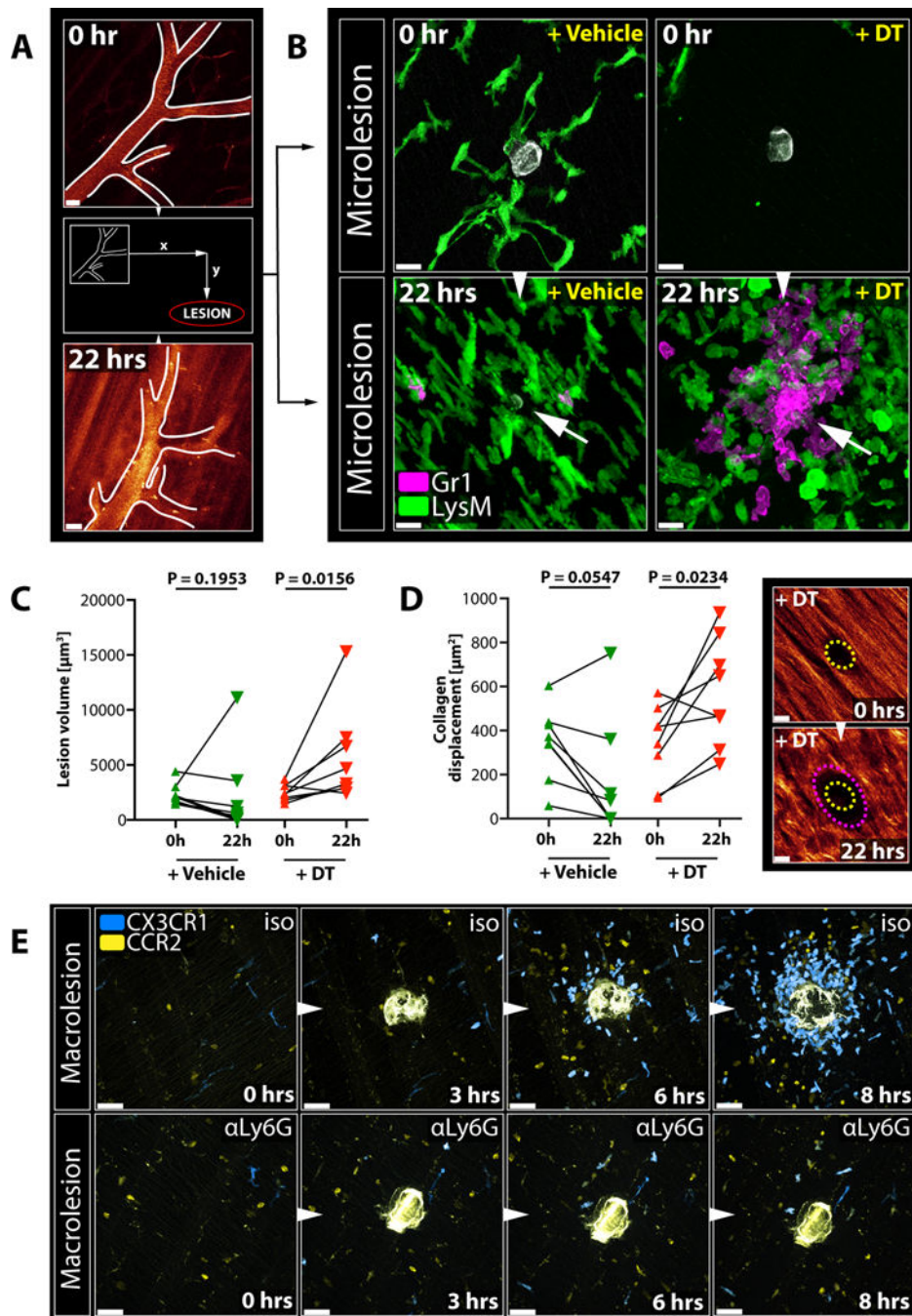


Figure 5. Failure of Cloaking Causes Collateral Damage and Requires Containment by Migratory Monocytes.

A) Vessel structure used as a reference point to map microlesions and re-image them 22 hours later. Scale bar, 30 µm.

B) RTM (green) and endogenous neutrophil responses (magenta) to microlesions (grey) right after damage induction and 22 hours later in CD169-DTR mice treated with vehicle (left) or DT (right). Arrows show late microlesions. Representative of 2 experiments. Scale bar, 20 µm.

C) Size changes of individual microlesions over time in vehicle-(left) or DT-treated CD169-DTR mice over time. Wilcoxon test on matched samples (n = 5–7). Representative of 2 experiments.

D) Collagen displacement at microlesions over time in vehicle-(left) or DT-treated CD169-DTR mice over time. Wilcoxon test on matched samples (n = 5–7 individual lesions). Representative of two independent experiments. Images show representative lesion in a DT-treated CD169-DTR mouse right after damage induction (top; yellow outline) and 22 hours later (bottom; magenta outline). Scale bar, 10 μm .

E) Dynamic response of migratory CX3CR1⁺ (blue) or CCR2⁺ (yellow) monocytes to a macro-lesion in isotype-treated (“iso”; top) or neutrophil-depleted (“ αLy6G ”; bottom) *Cx3cr1^{gfp/+}Ccr2^{gfp/+}* reporter mice. Scale bar, 30 μm . Representative of 3 experiments each. See Movie S5B.

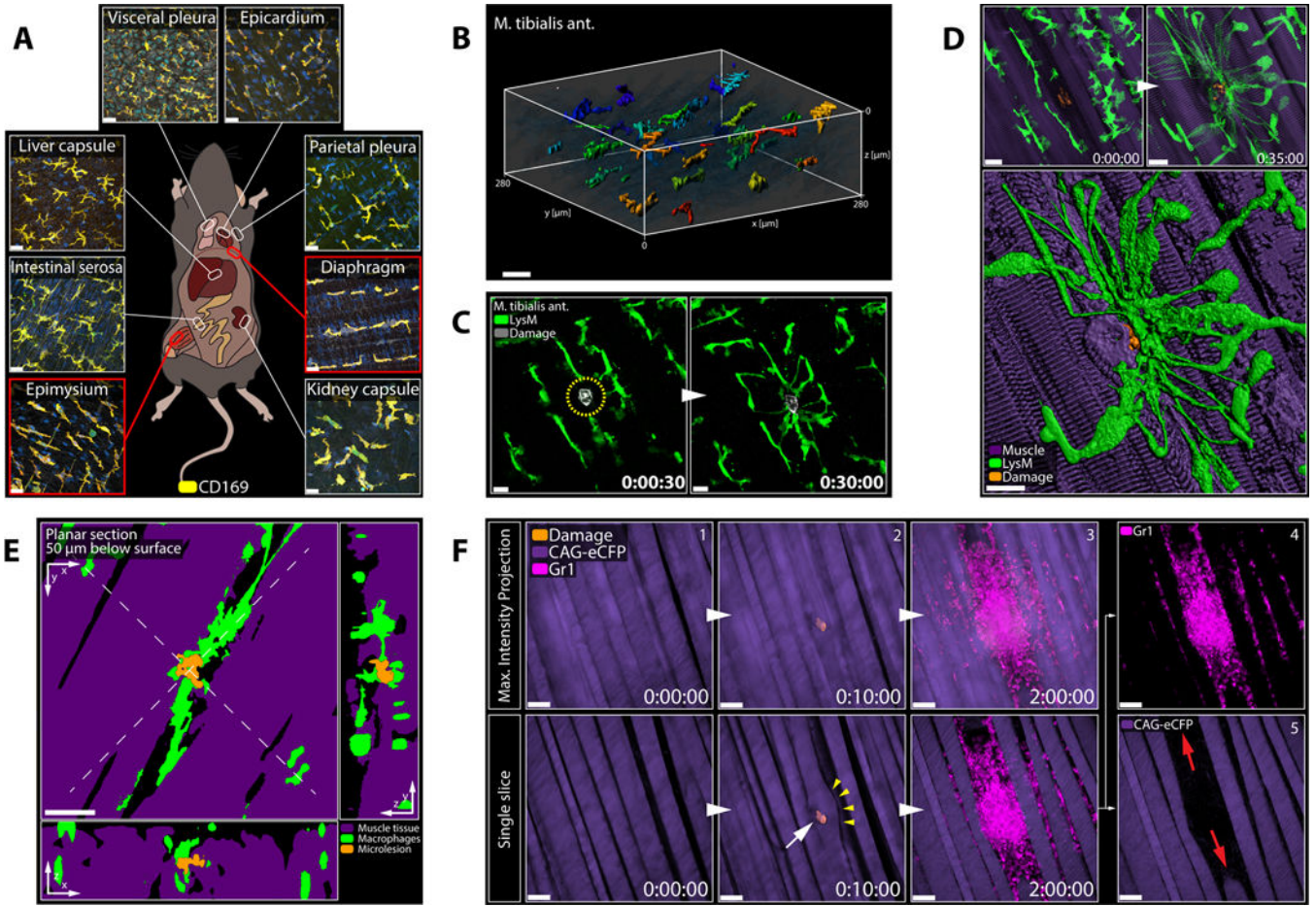


Figure 6. RTM Cloak Damaged Muscle Fibers.

A) Confocal images showing various RTM populations in naïve LysM-gfp mice.

Representative of 2 experiments. Scale bar, 30 μm .

B) 3D reconstruction of RTM distribution in the tibialis anterior muscle. Object color = distance on y-axis. Scale bar, 30 μm .

C) Endomysial RTM (green) responding to a microlesion (grey) in the tibialis anterior muscle. Scale bar, 20 μm . Representative of 3 experiments.

D) Endo- and perimysial RTM (green) responding to a partially damaged myofiber (top = max intensity projection; bottom = 3D reconstruction). See Data File S3A. Scale bar, 20 μm .

E) Planar cross sections of 3D object in Figure 6D. See Data File S3B. Scale bar, 20 μm .

F) Pre-recruited neutrophils (magenta) swarming at a partially damaged myocyte (purple).

Top = max intensity projection; bottom = single slice through plane of damage. Arrows show ruptured myofiber. Scale bar, 50 μm . Representative of 3 experiments.

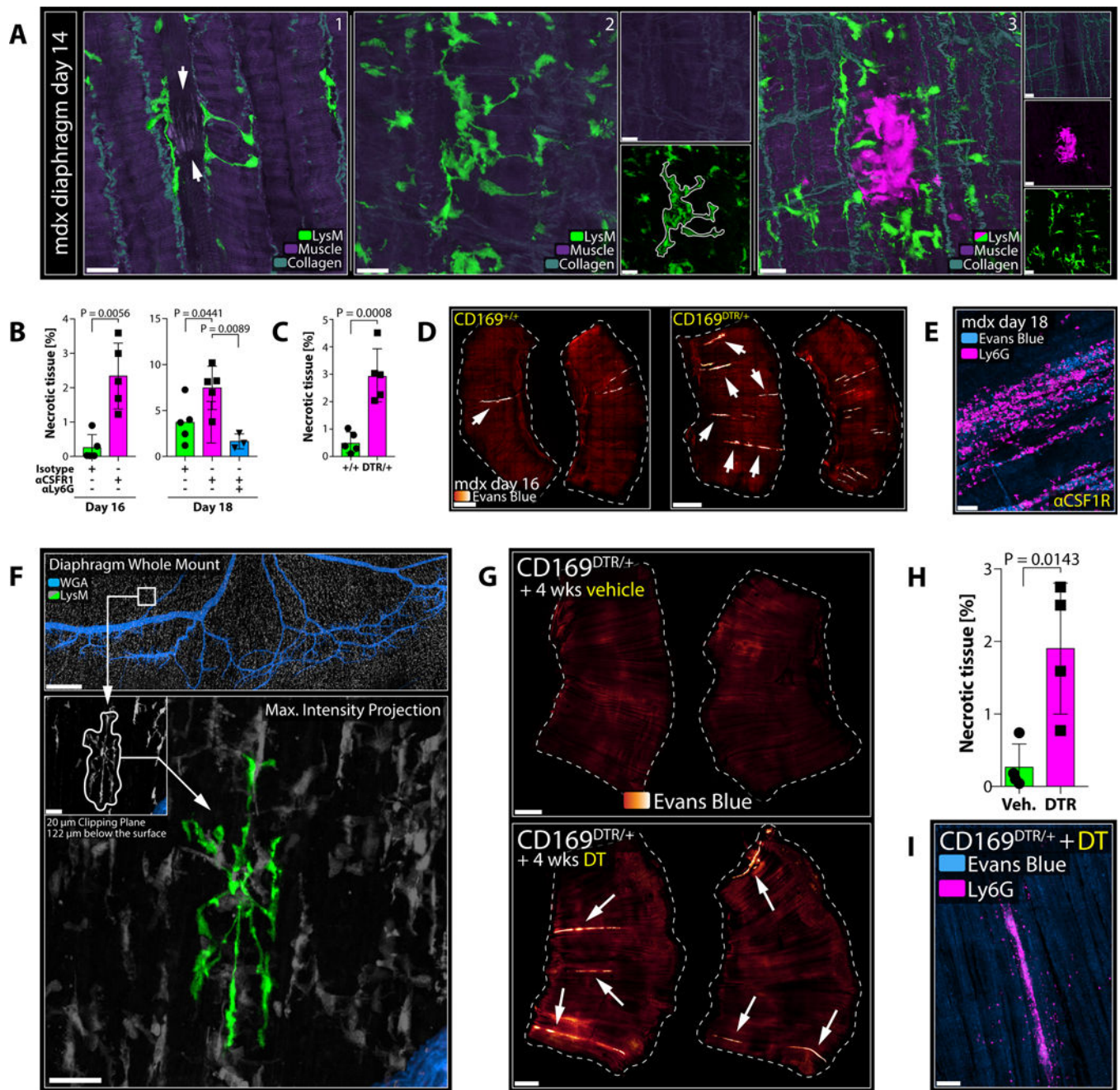


Figure 7. RTM Cloak Damaged Muscle Fibers.

A) Diaphragms isolated from mdx mice at day 14 of age. White arrows show damaged muscle fibre with cloaking RTM processes. Representative of > 3 experiments. Scale bar, 20 µm.

B) Extent of necrosis in diaphragms of mdx mice on day 16 (left) or day 18 (right), treated with isotype (green), anti-CSFR1 (magenta) or anti-CSFR1/anti-Ly6G (blue). Unpaired t test (day 16); one-way ANOVA (day 18); n = 3–5 animals per group; means ± SEM. Representative of 2 experiments.

- C) Extent of necrosis in diaphragms of CD169^{+/+} (green) or CD169^{DTR/+} (magenta) mdx mice on day 16, treated with DT. Unpaired t test; n = 5 animals per group; means \pm SEM. Representative of 2 experiments.
- D) Diaphragms from CD169^{+/+} or CD169^{DTR/+} mdx mice on day 16. Arrows show necrotic tissues (orange-to-white). Scale bar, 1000 μ m.
- E) Neutrophil infiltrates (magenta) in necrotic muscle (blue). Scale bar, 50 μ m.
- F) Representative confocal image of a Ce3D-cleared diaphragm; cloaking RTM highlighted in green. Scale bars, 500 μ m (top) and 30 μ m (bottom). See Movie S7A.
- G) Diaphragms from adult CD169-DTR mice after long-term treatment with vehicle (left) or DT (right). Arrows show necrotic tissues (orange-to-white). Scale bar, 1000 μ m.
- H) Quantification of necrosis in diaphragms of CD169-DTR mice after long-term treatment with vehicle (green) or DT (right). Unpaired t test; n = 4 animals per group; means \pm SEM. Representative of 2 experiments.
- I) Neutrophil infiltrates (magenta) in necrotic muscle (blue) in CD169-DTR mice after long-term DT-treatment. Scale bar, 100 μ m.

KEY RESOURCE TABLE

REAGENT or RESOURCE	SOURCE	IDENTIFIER
Antibodies		
Rat anti-mouse I-A/I-E Alexa Fluor 647; clone M5/114.15.2	BioLegend	Cat#107617
Rat anti-mouse/human CD11b Brilliant Violet 510; clone M1/70	BioLegend	Cat#101245
Rat anti-mouse CD45 Alexa Fluor 700; clone 30-F11	BioLegend	Cat#103127
Rat anti-mouse CD169 Alexa Fluor 647; clone 3D6.112	BioLegend	Cat#142407
Rat anti-mouse CD34 PE; clone HM34	BioLegend	Cat#128609
Rat anti-mouse Ly6G; clone 1A8	BioXCell	Cat#BE0075-1
Rat anti-mouse CSFR1; clone AFS98	BioXCell	Cat#BE0213
Rat anti-mouse Ly-6G FITC; clone 1A8	BioLegend	Cat#127605
Rat anti-mouse Ly-6G Alexa Fluor 647; clone 1A8	BioLegend	Cat#127621
Rat anti-mouse Ly-6G/Ly-6C (Gr-1) FITC; clone RB6-8C5	BioLegend	Cat#108405
Chemicals, Peptides, and Recombinant Proteins		
N-Methylacetamide	Sigma-Aldrich	Cat#M26305
Triton X-100	Sigma-Aldrich	Cat#T8787
Histodenz	Sigma-Aldrich	Cat#D2158
16% Paraformaldehyde (formaldehyde) aqueous solution	EMS	Cat#15710
TRIzol Reagent	Invitrogen	Cat#15596026
EDTA (0.5M), pH 8.0	Quality Biological	Cat#351-027-101
FBS: GemCell™ fetal bovine serum	Gemini	Cat#100-106 Lot# A20G001
Z-VAD-FMK	Tocris	Cat#2163
PBS, pH 7.4	Gibco	Cat#10010-23
HEPES (1M)	Gibco	Cat#15630080
DNAse II: Deoxyribonuclease II from bovine spleen Type V	Sigma-Aldrich	Cat#D8764
Liberase TL Research Grade low Thermolysin	Sigma-Aldrich	Cat#5401020001
RPMI 1640 Medium	Gibco	Cat#11875093
Dextran-Cascade Blue; 10 kDa	Invitrogen	Cat#D1976
Dextran-Fluorescein; 2000 kDa	Invitrogen	Cat#D7137
Dextran-Tetramethylrhodamine; 70 kDa	Invitrogen	Cat#D1818
BSA: Albumin from Bovine Serum (BSA), Alexa Fluor 647	ThermoFisher	Cat#A34785
BD Perm/Wash Buffer	BD Bioscience	Cat#554723
BD Cytotfix/Cytoperm Fixation/Permeabilization Solution Kit	BD Bioscience	Cat#554714
Zymosan: Zymosan A from <i>Saccharomyces cerevisiae</i>	Sigma-Aldrich	Cat#Z4250
Evans Blue: Evans Blue tetrasodium salt	Tocris	Cat#0845
DT: Diphtheria Toxin from <i>Corynebacterium diphtheriae</i>	Sigma-Aldrich	Cat#D0564
Clopidogrel: (±) Clopidogrel hydrogensulfate	Sigma-Aldrich	Cat#C0614
PT: Pertussis toxin from <i>Bordetella pertussis</i>	Sigma-Aldrich	Cat#P7208
RAP: RAGE antagonist peptide	Tocris	Cat#6259

REAGENT or RESOURCE	SOURCE	IDENTIFIER
FPS-ZM1	Tocris	Cat#6237
BzATP: 2' (3')-O-(4-Benzoylbenzoyl)adenosine 5'-triphosphate triethylammonium salt	Sigma-Aldrich	Cat#B6396
oxATP: Adenosine 5'-triphosphate, periodate oxidized sodium salt	Sigma-Aldrich	Cat#A6779
isoPPADS: iso-PPADS tetrasodium salt	Tocris	Cat#0683
JNJ 47965567	Tocris	Cat#5299
A438079 hydrochloride hydrate	Sigma-Aldrich	Cat#A9736
PSB12062	Sigma-Aldrich	Cat#SML0753
5-BDBD	Tocris	Cat#3579
Suramin: Suramin sodium salt	Sigma-Aldrich	Cat#S2671
PSB0739	Tocris	Cat#3983
MRS2578	Tocris	Cat#2146
Apyrase: Apyrase from potatoes	Sigma-Aldrich	Cat#A6535
Forane (isoflurane, USP)	Baxter	Cat#1001936040
Wheat Germ Agglutinin Alexa Fluor 488	ThermoFisher	Cat#W11261
Sodium chloride	Sigma-Aldrich	S5886
Potassium chloride	Sigma-Aldrich	P9333
Calcium chloride	Sigma-Aldrich	C5670
Magnesium Chloride	Sigma-Aldrich	M4880
Critical Commercial Assays		
Nugen Ovation SoLo RNA-Seq System	NuGEN	Cat#0501-32
Illumina NextSeq 500 High Output v2 Kit	Illumina	Cat#FC-404-2005
Amicon Ultracel-10K	Milipore	Cat#UFC501024
Deposited Data		
RNAseq data in this paper	NCBI GEO	CGSE119870
Experimental Models: Organisms/Strains		
LysM-gfp: C57BL/6-Lysozyme ^{tm1M-GFP} ; homozygous	Taconic Farms	Cat#000342
LysM-gfp het: C57BL/6NTac-Lysozyme ^{tm1M-GFP} ; heterozygous	Taconic Farms	Cat#008504
MaFIA: C57BL/6-Tg(<i>Csf1r</i> -EGFP-NGFR/FKBP1A/TNFRSF6)	The Jackson Laboratories	Cat#005070
CD68-gfp: C57BL/6-Tg(CD68-EGFP)1Drg/J	The Jackson Laboratories	Cat#026827
LysMcre: B6.129P2- <i>Lyz2</i> ^{m1(cre)lf0j}	The Jackson Laboratories	Cat#004781
Csf1r-DTR: C57BL/6-Tg(<i>Csf1r</i> -HBEGF/mCherry)1Mnz/J	The Jackson Laboratories	Cat#024046
tdTom: B6.Cg- <i>Gt(ROSA)26Sor</i> ^{tm14(CAG-tdTomato)Hze/J}	The Jackson Laboratories	Cat#007914
LysMcre: B6N.129P2(B6)- <i>Lyz2</i> ^{m1(cre)lf0j}	The Jackson Laboratories	Cat#018956
CD169-DTR: B6;129- <i>Siglec1</i> <tm1(HBEGF)Mtk	Developed by Makoto Tanaka (Miyake et al., 2007; Tokyo University, Tokyo, Japan); distributed through RIKEN BRC (Tokyo, Japan); provided by Tracy McGaha (University of Toronto, Toronto, Canada); MTA with RIKEN in place.	Cat#RBRC04395
CX3CR1-gfp: C57BL/6-CD45a-[KO]CX3CR1-[KI]EGFP	Taconic Farms	Cat#008455
CCR2-rfp: B6.129(Cg)- <i>Ccr2</i> ^{m2.1lf0j}	The Jackson Laboratories	Cat#017586

REAGENT or RESOURCE	SOURCE	IDENTIFIER
Mdx: C57BL/10ScSn- <i>Dmd</i> ^{mdx} /J	The Jackson Laboratories	Cat#001801
RAGE ^{-/-} or RAGE ^{-/-} .eGFP: <i>Age1</i> ^{tm1.1Amd}	Developed by Bernd Arnold (Constien et al., 2001; German Cancer Research Center, Heidelberg, Germany); provided by Ann Marie Schmidt (NYU School of medicine, New York, USA); MTA with NYU in place.	RRID:MGI:3694549
Software and Algorithms		
Leica Application Suite X (LAS X)	Leica Microsystems	RRID:SCR_013673
ZEN Digital Imaging for Light Microscopy, ZEN 2012	Zeiss	RRID:SCR_013672
Huygens Professional, version 18.04	Scientific Volume Imaging	RRID:SCR_014237
Imaris, versions 8.6–9.3	Bitplane	RRID:SCR_007370
GraphPad Prism, version 7	GraphPad Software	RRID:SCR_002798
R Project for Statistical Computing, version 3.5.1	https://cran.r-project.org/	RRID:SCR_001905
MeshLab, version 2016.12	ISTI-CNR; http://www.meshlab.net/	N/A
Adobe Photoshop CC 2018–2019	Adobe	RRID:SCR_014199
Adobe Illustrator CC 2018–2019	Adobe	RRID:SCR_010279)
Adobe Premiere Pro CC 2018–2019	Adobe	N/A
Adobe After Effects CC 2018–2019	Adobe	N/A
Adobe Media Encoder CC 2018–2019	Adobe	N/A
Adobe Acrobat Pro DC	Adobe	N/A
Salmon, version 0.11.3	Developed by Carl Kingsford (Carnegie Mellon University, Pittsburgh, USA); https://github.com/COMBINE-lab/salmon	N/A
Tximport, version 1.4.0	Developed by Mark Robinson (University of Zurich, Switzerland); https://bioconductor.org/packages/release/bioc/html/tximport.html	RRID:SCR_016752
org.Mm.eg.db database, version 3.4.1	Developed by Marc Carlson (Fred Hutchinson Research Center, Seattle, USA); https://bioconductor.org/packages/release/data/annotation/html/org.Mm.eg.db.html	N/A
Other		
Vetbond	3M	Cat#1469SB
Monomid 5/0 Nylon	CP Medical	Cat#661B
Fisherbrand Cover Glasses: Circles	Fisher Scientific	Cat#12–545-80